A study on a numerical analysis method for nonlinear optical channel waveguides and its applications

Akira NIIYAMA

(1)

A study on a numerical analysis method for nonlinear optical channel waveguides and its applications

Akira NIIYAMA

Contents

1 Preface

After the emergence of lasers as a coherent light source and the practical use of optical fibers as a communication channel, optoelectronics has been playing an important role in the field of telecommunication and information processing technology. And nowadays, the discovery and experimental inspection of optical fiber soliton, and its application to communication systems show the importance of nonlinear optics, and made a considerable contribution toward the foundation of the field called the nonlinear guided-wave optics. There are increasing interests in unique features of nonlinear waves guided not only in fibers but in various nonlinear optical waveguides.

In addition, as a novel technology for the breakthrough of the limitation of electro-optical and opto-electric conversions in the conventional optical signal processing, there are considerably increasing interests in "all-optical signal processing", unique features of nonlinear guided waves, and the application to optical bistable devices and optical logic gates. In these backgrounds, the analysis technique for the nonlinear optical fibers and waveguides is the most important for design of all-optical signal processing devices.

Most papers concerned with modal analysis of nonlinear optical waveguides have dealt with a planar guiding structure in which optical power is confined solely along one direction (y axis). For practical applications, however, there may be advantages in using a channel guiding structure in which optical power is confined along the lateral direction (x axis) as well as the y direction.

Recently, an effective index method (EIM) [1], [2] and a vector or scalar finite element method (FEM) [3]–[8] have been applied to modal analysis of nonlinear optical channel waveguides. Although the calculational procedure of the EIM is relatively simple, it seems to be difficult to treat arbitrarily shaped and/or inhomogeneous structures. On the other hand, the FEM is more effective for precise investigation. In comparison with the vector finite element analysis with penalty function method [3]–[7] for the elimination of the nonphysical spurious solutions, the scalar FEM approach [5], [8] has as its main advantages: the smaller matrix dimensions, no spurious solutions, and capability of easily computing the propagation

constant at a specified frequency. In [5], [8], however, only the TE-like polarization is considered.

In Chapter 2, a self-consistent numerical approach based on the scalar finite element method is described for the analysis of both TE-like and TM-like nonlinear guided waves in optical channel waveguides. In order to improve the convergence and accuracy of solutions, isoparametric elements and numerical integration formulae derived by Hammer *et al.* are introduced. Numerical results are presented for nonlinear elliptical core optical fibers, and it is confirmed that in this approach, highly accurate solutions can be obtained with small scale computation. Furthermore, graded-index nonlinear optical channel waveguides are also analyzed, and the influence of refractive-index profiles on propagation characteristics of the nonlinear guided waves is investigated.

Recently, some papers concerned with the modal [9] and/or beam propagation analyses [10] of nonlinear optical waveguides have dealt with a symmetric planar guiding structure which is composed of thin film embedded in intensity-dependent nonlinear media, and have shown the phenomena peculiar to nonlinear guided waves, such as symmetry-breaking behaviour, existence of symmetric/asymmetric modes, spatial soliton emission, and so on. Modal characteristics of a nonlinear optical fiber with nonlinear cladding have also been analyzed [11], [12], and axially symmetric modes [11] whose field profiles are similar to surface wave modes and asymmetric modes [12] whose field profiles have no axial symmetry have been found. However, the excitation and the stability of these interesting stationary modes have been quite rarely investigated.

In Chapter 3, a 3-dimensional beam propagation method is described for the analysis of nonlinear optical fibers, where the finite element and finite difference methods are, respectively, utilized for discretizing the fiber cross section and the propagation direction. The application of certain techiniques for differential operation and numerical integration makes the improvement of the efficiency and accuracy of solutions. The propagation characteristics of nonlinear optical fibers with linear core and nonlinear cladding are analyzed, and unique features of nonlinear guided-wave propagation are investigated. Furthermore, all-optical logic gates with practical, 3-dimensional geometry consisting of optical fibers and a non-

linear film are proposed, and their operations of Boolean arithmetric are demonstrated.

The use of the approximate scalar theory [13], [14] would be possible under certain restrictions on magnitudes of nonlinearities and optical intensities. Recently the finite element method with nodal elements has been applied to optical channel waveguides with Kerr and/or Kerr-like nonlinearities, based on the rigorous vectorial approach [15]–[20]. The most serious problem associated with the vectorial finite element approach, on the other hand, is the appearance of spurious solutions, and the other serious problem is that it is quite difficult for dealing with corner and interface singularities so long as conventional nodal elements are used to approximate vector fields.

In Chapter 4, a self-consistent full-vectorial approach based on the finite element method with edge/nodal hybrid element [21], [22] which is introduced to cure the problems mentioned above is described for the modal analysis of nonlinear optical channel waveguides, and an application of conventional scalar field theory to the prediction of modal properties of both TE-like and TM-like nonlinear guided modes is examined. Numerical results are presented for nonlinear optical fibers, strip-loaded nonlinear optical channel waveguides, and multiple-quantum-well-embedded nonlinear optical channel waveguides. Serious limitations on the validity of the scalar field approximation are found in the high power regime, where nonlinearities are expected to play an essential role in forming the stationary mode.

The 3-dimensional beam propagation analysis with approximated-scalar finite-element and finite-difference methods, described in Chapter 3 of this paper, is available under the assumption of the nonlinear guided wave as a scalar field. When the guided wave in strong-nonlinearity and high-power regime, however, exceeds the limit of the approximation, the full-vectorial beam propagation analysis is absolutely essential. Recent papers [23]–[25] propose the analysis based on the vector finite element beam propagation method. The proposed approach is based on the hybrid element which is also utilized in Chapter 4 for waveguides' transverse direction and the wide-angle finite difference method with backward scheme for the propagation direction. These papers demonstrate the beam propagation in nonlinear bulk media, nonlinear slab waveguides, and the emergence of

optical vortex soliton in the cylindrical waveguides filled by self-defocusing nonlinear media. The proposed approach reveals the fascinating feature of nonlinear optical effects, however, there is room for progress of computational efficiency, taking the practical use for computer aided design of nonlinear optical devices into account.

In Chapter 5, in order to improve the efficiency and accuracy, the calculational technique for numerical integration is newly applied to the 3-dimensional full-vectorial finite-element beam propagation method. For the efficient wide-angle beam propagation analysis, Padé approximation is introduced to the differential operation along propagation direction. The formulation of this proposed approach is described in detail.

The conclusions of this paper are described in Chapter 6.

2 Approximated Scalar Finite Element Analysis of 3-Dimensional Nonlinear Optical Wavegudes

2.1 Introduction

Nonlinear optical waveguides have attracted considerable attention because of their fascinating features and their use in all-optical signal processing. Most papers concerned with modal analysis of nonlinear optical waveguides have dealt with a planar guiding structure in which optical power is confined solely along one direction (y axis). For practical applications, however, there may be advantages in using a channel guiding structure in which optical power is confined along the lateral direction (x axis) as well as the y direction.

Recently, an effective index method (EIM) [1], [2] and a vector or scalar finite element method (FEM) [3]–[8] have been applied to modal analysis of nonlinear optical channel waveguides. Although the calculational procedure of the EIM is relatively simple, it seems to be difficult to treat arbitrarily shaped and/or inhomogeneous structures. On the other hand, the FEM is more effective for precise investigation. However, the vector finite element solutions [3]–[7] have been known to include nonphysical, spurious solutions. The penalty function method has been used to cure this problem [3]–[7], but in this technique, an arbitrary positive constant, called the penalty coefficient, is involved, and the accuracy of solutions depends on its magnitude. Furthermore, it is difficult to yield the matrix eigenvalue equation to solve for the propagation constant, so iterations are usually needed to find the propagation constant at a specified frequency. Although the scalar FEM [5], [8] is approximate in a strict sense, this approach has as its main advantages: the smaller matrix dimensions, no spurious solutions, and capability of easily computing the propagation constant at a specified frequency. In [5], [8], however, only the TE-like polarization is considered.

By the way, in the earlier finite element analyses of nonlinear optical channel waveguides [3]–[8], the intensity-dependent refractive index is assumed to be constant within each element. Hence, if the accuracy of solutions needs to be improved, the scale of computation becomes significantly large. For instance, in [4], [8] about 1000 linear triangular elements

are used to obtain sufficiently converging solutions.

In this chapter, with a view to improving the efficiency of the scalar FEM which is considered effective for the analysis and design of nonlinear optical channel waveguides, isoparametric elements are introduced, and the use of numerical integration formulae derived by Hammer *et al.* [26], [27] is attempted for the calculation of integrals necessary for constructing element matrices. Both TE-like and TM-like guided waves are treated. By means of this approach, the refractive index change within each element can be faithfully evaluated according to the electric field distribution without fixing the index constant in each element, and the graded-index nonlinear optical waveguides with curved boundaries can also be easily treated. Nonlinear elliptical core optical fibers are, for the first time, analyzed. It is found that, in comparison to the conventional method without isoparametric elements, the highly accurate solutions can be obtained with substantially smaller computational effort. Furthermore, graded-index nonlinear optical channel waveguides are also analyzed, and the influence of refractive-index profiles on propagation characteristics of the nonlinear guided waves is investigated. To date, all the papers concerned with modal analysis of graded-index nonlinear optical waveguides have dealt with only the planar guiding structures [28]–[33].

2.2 Basic Equations

We consider a nonlinear optical channel waveguide with arbitrary cross section in the xy plane and assume that the structure is uniform along the propagation direction (z axis). From Maxwell's equations, the following Helmholtz equation is derived under the assumption of a vanishing parasitic electric or magnetic field component, $E_y \equiv 0$ for the TE-like, E^x modes (main fields are E_x and H_y) and $H_y \equiv 0$ for the TM-like, E^y modes (main fields are E_y and H_x) [27], [34]:

$$p\frac{\partial^2\phi}{\partial x^2} + p\frac{\partial^2\phi}{\partial y^2} + qk_0^2\phi - p\beta^2\phi = 0 \tag{1}$$

where k_0 is the free space wavenumber, β is the propagation constant along z axis, and the main field $\phi(x, y)$ and coefficients p, q are written as

$$\phi = E_x,\ p = 1,\ q = n^2 \tag{2}$$

for E^x modes, and

$$\phi = H_x,\ p = 1/n^2,\ q = 1 \tag{3}$$

for E^y modes. Assuming electrostrictive and thermal nonlinearities [7] which are usually supposed in modal analysis of nonlinear optical waveguides, the intensity-dependent refractive index n is given by

$$n = n(x, y\ ;\ \ |\boldsymbol{E}|^2). \tag{4}$$

The electric field vector $\boldsymbol{E}$ used in (4) is approximated as

$$\boldsymbol{E}{=}E_x \boldsymbol{i}_x + E_z \boldsymbol{i}_z \tag{5a}$$

$$E_x{=}\phi,\ E_z = -j\frac{1}{n_{eff}}\phi',\ \phi' = \frac{\partial \phi}{\partial \bar{x}} \tag{5b}$$

for E^x modes, and

$$\boldsymbol{E}{=}E_y \boldsymbol{i}_y + E_z \boldsymbol{i}_z \tag{6a}$$

$$E_y{=}-\frac{n_{eff} Z_0}{n^2}\phi,\ E_z = -j\frac{Z_0}{n^2}\phi',\ \phi' = \frac{\partial \phi}{\partial \bar{y}} \tag{6b}$$

for E^y modes. Here $\boldsymbol{i}_x$, $\boldsymbol{i}_y$, and $\boldsymbol{i}_z$ are the unit vectors in the x, y, and z directions, respectively, $\bar{x}$ and $\bar{y}$ are the Cartesian coordinates normalized by the free space wavenumber, namely, $\bar{x} = k_0 x$ and $\bar{y} = k_0 y$, n_{eff} is the effective refractive index defined as $n_{eff} \equiv \beta / k_0$, and Z_0 is the free space impeadance.

In the case of a planar optical waveguide ($\partial/\partial x \equiv 0$) the above equations for the E^x and E^y modes give exact expressions for truely TE and TM polarizations, respectively.

2.3 Finite Element Discretization

We divide the waveguide cross section into a number of isoparametric triangular elements as shown in Fig. 1, where closed circles 1 to 6 denote nodal points and open circles 1 to 7 denote sampling points used for numerical integration. In the isoparametric element the polynomial order representing the geometry of an element is coincident with that interpolating the field in an element. In the quadratic isoparametric element in

Fig. 1 the field ϕ and the normalized Cartesian coordinates $\bar{x}$, $\bar{y}$ can be expanded as

$$\phi = \{N\}^T \{\phi\}_e \tag{7}$$

$$\bar{x} = \{N\}^T \{\bar{x}\}_e \tag{8}$$

$$\bar{y} = \{N\}^T \{\bar{y}\}_e \tag{9}$$

with

$$\{N\} = \begin{bmatrix} L_1(2L_1 - 1) \\ L_2(2L_2 - 1) \\ L_3(2L_3 - 1) \\ 4L_1L_2 \\ 4L_2L_3 \\ 4L_3L_1 \end{bmatrix} \tag{10}$$

where $\{\phi\}_e$ and $\{\bar{x}\}_e$, $\{\bar{y}\}_e$ are, respectively, the electric or magnetic field and the normalized Cartesian coordinate vectors corresponding to the nodal points 1 to 6 within each element e, $\{N\}$ is the shape function vector, L_1, L_2, L_3 are the area coordinates, and T denotes a transpose.

Defining the local coordinates ξ, η as

$$L_1 = \xi, \; L_2 = \eta, \; L_3 = 1 - \xi - \eta \tag{11}$$

the transformation for differentiation is given by

$$\begin{bmatrix} \partial/\partial\xi \\ \partial/\partial\eta \end{bmatrix} = [J] \begin{bmatrix} \partial/\partial\bar{x} \\ \partial/\partial\bar{y} \end{bmatrix} = \begin{bmatrix} J_{11} & J_{12} \\ J_{21} & J_{22} \end{bmatrix} \begin{bmatrix} \partial/\partial\bar{x} \\ \partial/\partial\bar{y} \end{bmatrix} \tag{12}$$

with

$$J_{11} = \partial\bar{x}/\partial\xi = \{N_\xi\}^T \{\bar{x}\}_e \tag{13a}$$

$$J_{12} = \partial\bar{y}/\partial\xi = \{N_\xi\}^T \{\bar{y}\}_e \tag{13b}$$

$$J_{21} = \partial\bar{x}/\partial\eta = \{N_\eta\}^T \{\bar{x}\}_e \tag{13c}$$

$$J_{22} = \partial\bar{y}/\partial\eta = \{N_\eta\}^T \{\bar{y}\}_e \tag{13d}$$

where $[J]$ is the Jacobian matrix and $\{N_\xi\} \equiv \partial\{N\}/\partial\xi$, $\{N_\eta\} \equiv \partial\{N\}/\partial\eta$.

The transformation relation for integration of the function $f(\bar{x}, \bar{y})$ is given by

$$\iint_e f(\bar{x}, \bar{y}) d\bar{x} d\bar{y} = \int_0^1 \int_0^{1-\xi} f(\xi, \eta) |J| d\xi d\eta \tag{14}$$

where $|J|$ is the determinant of the Jacobian matrix and is known as the Jacobian.

Using (12), ϕ' in (5b), (6b) is expressed as

$$\phi' = |J|^{-1}(J_{22}\{N_\xi\}^T - J_{12}\{N_\eta\}^T)\{\phi\}_e \tag{15}$$

for E^x modes, and

$$\phi' = |J|^{-1}(-J_{21}\{N_\xi\}^T + J_{11}\{N_\eta\}^T)\{\phi\}_e \tag{16}$$

for E^y modes.

Applying the finite element technique to (1), we obtain

$$[K(\phi)]\{\phi\} = n_{eff}^2 [M(\phi)]\{\phi\} \tag{17}$$

with

$$\begin{aligned}[K(\phi)] = \sum_e \iint_e [& q_e(\bar{x}, \bar{y}; \phi, \phi')\{N\}\{N\}^T \\ & - p_e(\bar{x}, \bar{y}; \phi, \phi')\{N_{\bar{x}}\}\{N_{\bar{x}}\}^T \\ & - p_e(\bar{x}, \bar{y}; \phi, \phi')\{N_{\bar{y}}\}\{N_{\bar{y}}\}^T] d\bar{x} d\bar{y}\end{aligned} \tag{18}$$

$$[M(\phi)] = \sum_e \iint_e p_e(\bar{x}, \bar{y}; \phi, \phi')\{N\}\{N\}^T d\bar{x} d\bar{y} \tag{19}$$

where the components of the $\{\phi\}$ vector are the values of ϕ at all nodal points, $\{N_{\bar{x}}\} \equiv \partial\{N\}/\partial\bar{x}$, $\{N_{\bar{y}}\} \equiv \partial\{N\}/\partial\bar{y}$, and $\sum_e$ extends over all different elements.

Noting (7)–(16), the integrants in (18) and (19) are given as the functions of the area coordinates, and thus, the numerical integration formulae derived by Hammer *et al.* [26], [27] can be directly applied. The integral calculations needed for constructing the matrices $[K]$ and $[M]$ can be replaced with simple product-sum calculations as

$$\begin{aligned}[K(\phi)] = \sum_e \sum_{i=1}^{7} \frac{1}{2} W_i |J|_i [& q_e(\bar{x}_i, \bar{y}_i; \phi_i, \phi_i')\{N\}_i\{N\}_i^T \\ & - p_e(\bar{x}_i, \bar{y}_i; \phi_i, \phi_i')\end{aligned}$$

TABLE I
THE VALUES OF THE WEIGHTING COEFFICIENTS AND AREA COORDINATES

i	W_i	(L_{1i}, L_{2i}, L_{3i})	
1	0.225	(α, α, α)	
2	0.13239415	(β, γ, γ)	α=1/3
3	0.13239415	(γ, β, γ)	β=0.05971587
4	0.13239415	(γ, γ, β)	γ=0.47014206
5	0.12593918	$(\delta, \epsilon, \epsilon)$	δ=0.79742669
6	0.12593918	$(\epsilon, \delta, \epsilon)$	ϵ=0.10128651
7	0.12593918	$(\epsilon, \epsilon, \delta)$	

$$\begin{aligned}
&\times|J|_i^{-2}(J_{22i}\{N_\xi\}_i - J_{12i}\{N_\eta\}_i)\\
&\times(J_{22i}\{N_\xi\}_i^T - J_{12i}\{N_\eta\}_i^T)\\
&-p_e(\bar{x}_i, \bar{y}_i; \phi_i, \phi_i')\\
&\times|J|_i^{-2}(-J_{21i}\{N_\xi\}_i + J_{11i}\{N_\eta\}_i)\\
&\times(-J_{21i}\{N_\xi\}_i^T + J_{11i}\{N_\eta\}_i^T)] \qquad (20)
\end{aligned}$$

$$[M(\phi)]=\sum_e \sum_{i=1}^{7} \frac{1}{2} W_i |J|_i p_e(\bar{x}_i, \bar{y}_i; \phi_i, \phi_i')\{N\}_i\{N\}_i^T \qquad (21)$$

where the subscript i (i=1, 2, $\cdots$, 7) denotes the quantity associated with the sampling point i, the values of the weighting coefficient W_i and the area coordinates L_{1i}, L_{2i}, L_{3i} are presented in Table I[26], [27].

The total guided wave power is evaluated as

$$P = \frac{1}{2}\iint_{-\infty}^{\infty} E_x H_y^* dxdy = \frac{n_{eff}}{2Z_0}\iint_{-\infty}^{\infty} |\phi|^2 dxdy \qquad (22)$$

for E^x modes, and

$$P = \frac{1}{2}\iint_{-\infty}^{\infty} -E_y H_x^* dxdy = \frac{n_{eff} Z_0}{2}\iint_{-\infty}^{\infty} \frac{|\phi|^2}{n^2} dxdy \qquad (23)$$

for E^y modes [27].

To obtain the intensity-dependent refractive index, it is necessary to compute the actual field ϕ without normalization. The relation between the actual (ϕ) and the normalized ($\bar{\phi}$) fields can be written as

$$|\phi| = k_0\sqrt{2Z_0P/n_{eff}}|\bar{\phi}| \tag{24}$$

for E^x modes, and

$$|\phi| = k_0\sqrt{2P/(n_{eff}Z_0)}|\bar{\phi}| \tag{25}$$

for E^y modes, where the usual normalization procedure of the eigenvector of (17)

$$\iint_{-\infty}^{\infty} p|\bar{\phi}|^2 d\bar{x}d\bar{y} = \{\bar{\phi}\}^T[M(\phi)]\{\bar{\phi}\} = 1 \tag{26}$$

is considered.

Equation (17) is a nonlinear generalized eigenvalue problem whose eigenvalue and eigenvector correspond to n_{eff}^2 and $\{\bar{\phi}\}$, respectively. Hence, one can solve it self-consistently using the following iterative scheme:

1) Specify the refractive index n, the wavelength $\lambda = 2\pi/k_0$, and optical power P as input data.

2) Assign initial values to n_{eff} and $\{\bar{\phi}\}$.

3) To obtain the nonlinear coefficient matrices $[K(\phi)]$ and $[M(\phi)]$, calculate $\{\phi\}$ and n.

4) To obtain a new set of n_{eff} and $\{\bar{\phi}\}$, solve the matrix eigenvalue equation (17).

5) Iterate the above procedures 2), 3), and 4) until the solution (eigenvalue) converges within the desired criterion.

Optical power specified in this iterative scheme is increased or decreased between a certain range with appropriate intervals. For the linear case, the solution can be obtained without assigning initial values, and for the nonlinear case, the initial values at each optical power are assigned to the convergent solutions calculated at the previous power. These initial values differ between increasing and decreasing powers, and thus, the above iteration scheme can evaluate the hysteresis nature of nonlinear optical waveguides as described later.

2.4 Numerical Results

A. Nonlinear Elliptical Core Fibers

As a nonlinear optical waveguide with curved boundaries, we consider a nonlinear elliptical core optical fibers as shown in Fig. 2. Here, for the symmetric, fundamental modes, namely, E_{11}^x and E_{11}^y modes, we subdivide one-quarter of the waveguide cross section into isoparametric elements. Four profiles of finite element mesh division are considered, all of which are shown in Fig. 3, where N_e is the number of elements, and the Neumann condition ($\partial\phi/\partial n = 0$, where $\partial/\partial n$ is the outward normal derivative) is imposed on all the boundaries AB, BC, CD, and DA. The Dirichret condition ($\phi = 0$) can also be utilized on the boundaries BC and CD which are located far from the core region, however, the difference between the results obtained by using the Neumann and Dirichret conditions is undistinguishable.

Figure 4(a) shows power dispersion curves for an elliptical core optical fiber with Kerr nonlinearity in the core and cladding, where the wavelength $\lambda = 0.632\mu$m and the following waveguide parameters are used:

$$\begin{aligned} a&=\sqrt{2}\ \mu\text{m}\ ,\ b = 1/\sqrt{2}\ \mu\text{m} \\ n_1&=n_{10}[1 + n'|\boldsymbol{E}|^2/(2Z_0)] \\ n_2&=n_{20}[1 + n'|\boldsymbol{E}|^2/(2Z_0)] \\ n_{10}&=1.466,\ n_{20} = 1.45,\ n' = 3.2 \times 10^{-20}\ \text{m}^2/\text{W}. \end{aligned}$$

Here n' is the nonlinear optical coefficient.

Figure 4(b) shows power dispersion curves for an elliptical core optical fiber with Kerr nonlinearity in the core, where the wavelength $\lambda = 0.5145\mu$m and the following waveguide parameters are used:

$$\begin{aligned} a&=\sqrt{2}\ \mu\text{m}\ ,\ b = 1/\sqrt{2}\ \mu\text{m} \\ n_1&=n_{10}[1 + n'|\boldsymbol{E}|^2/(2Z_0)] \\ n_2&=n_{20} \\ n_{10}&=1.57,\ n_{20} = 1.55,\ n' = 10^{-9}\ \text{m}^2/\text{W}. \end{aligned}$$

At low optical power, the results of the earlier approach using conventional quadratic triangular elements with straight sides agree well with those of the present approach using isoparametric triangular elements. When the power is higher, however, a significant discrepancy is observed.

In the present approach the convergence of solutions is very fast irrespective of the polarization and the magnitude of the nonlinearity, and highly accurate results can be obtained without increasing the computational effort. It is found from Figs. 4(a) and (b) that the modal birefringence is greatly enhanced with increasing optical power.

We have found that in case of $a = b$, namely a circular core optical fiber, the results of the present approach are in good agreement with analytical solutions [35]. It is interesting to note that the power dispersion curve for the E_{11}^x mode of an elliptical core fiber ($a = \sqrt{2}\mu$m and $b = 1/\sqrt{2}\mu$m) is similar to that for the LP_{01} mode of a circular core fiber with the same core area ($a = b = 1\mu$m).

B. Graded-Index Nonlinear Channel Waveguides

We consider a graded-index nonlinear optical channel waveguide as shown in Fig. 5, where the wavelength $\lambda = 0.515\mu$m and the following waveguide parameters are used:

$$
\begin{aligned}
t&=1.0\ \mu\text{m}\\
n_f&=n_{f0}+\Delta n_{sat}\{1-\exp[-n_{f0}n'|\boldsymbol{E}|^2/(2\Delta n_{sat}Z_0)]\}\\
n_s&=n_{s0}+\Delta n f(x)g(y)\\
n_c&=n_{c0}\\
n_{f0}&=1.55,\ n_{s0}=1.55,\ n_{c0}=1.0\\
\Delta n&=0.02,\ \Delta n_{sat}=0.04,\ n'=10^{-9}\ \text{m}^2/\text{W}.
\end{aligned}
$$

Here the nonlinearity is produced by a saturable system. The refractive index profile in the substrate region is assumed to be

$$
\begin{aligned}
f(x)&=\exp[-(x/d_x)^2]\\
g(x)&=\exp(-y/d_y)
\end{aligned}
$$

for 'type 1' with Gaussian and exponential profiles in the x and y directions, respectively,

$$
\begin{aligned}
f(x)&=\exp[-(x/d_x)^2]\\
g(x)&=\exp[-(y/d_y)^2]
\end{aligned}
$$

for 'type 2' with Gaussian profiles in both the directions, and

$$
\begin{aligned}
f(x)&=u(x+d_x)-u(x-d_x)\\
g(x)&=u(y)-u(y-d_x)
\end{aligned}
$$

for 'type 3' with step-index profiles in both the directions, where u is the unit-step function, and d_x and d_y are the diffusion lengths in the x and y directions, respectively. A typical element division is shown in Fig. 6, and the Neumann condition is imposed on all the boundaries AB, BC, CD, and DA.

Figures 10(a) and (b) show power dispersion curves of the E_{11}^x and the E_{11}^y modes, respectively, where d_x=d_y=3μm. The change in the effective index with optical power is initially slower, but above a certain threshold the mode moves abruptly from the linear substrate into the nonlinear film causing a jump in the effective index. The threshold power of the graded-index waveguide (type 1 or 2) is much lower than that of the step-index one (type 3). When decreasing optical power, the dispersion curve exhibits the hysteresis nature and the mode returns abruptly to the linear substrate. The threshold power becomes higher and the width of the hysteresis loop becomes also larger in the order, type 1, type 2, and type 3. The hysteresis loop for the step-index waveguide is significantly different between the E_{11}^x and the E_{11}^y modes.

Figure 8 shows the proportions of optical power carried by the film and substrate regions for the E_{11}^x and E_{11}^y modes, respectively. Only negligible power propagates through the cover region. When optical power increases (or decreases), beyond the threshold power, suddenly most of the power moves to the film (or substrate) and the power inside the substrate (or film) falls drastically.

2.5 Conclusion

We have formulated an efficient approach based on the scalar finite element method for the analysis of nonlinear optical channel waveguides. Both TE-like and TM-like modes have been treated, and in order to improve the convergence and accuracy of solutions, isoparametric elements and numerical integration formulae derived by Hammer *et al.* have been introduced. Numerical results have been presented for nonlinear elliptical core optical fibers and graded-index nonlinear optical channel waveguides.

For the numerical advantage, we have used the symmetry of nonlinear waveguides, however, it should be noted that its use can exclude some modes which may be allowable in nonlinear waveguides. Although the

modal solutions provide useful information about the nonlinear properties of the guided waves, more involved beam propagation analysis is needed in a practical situation.

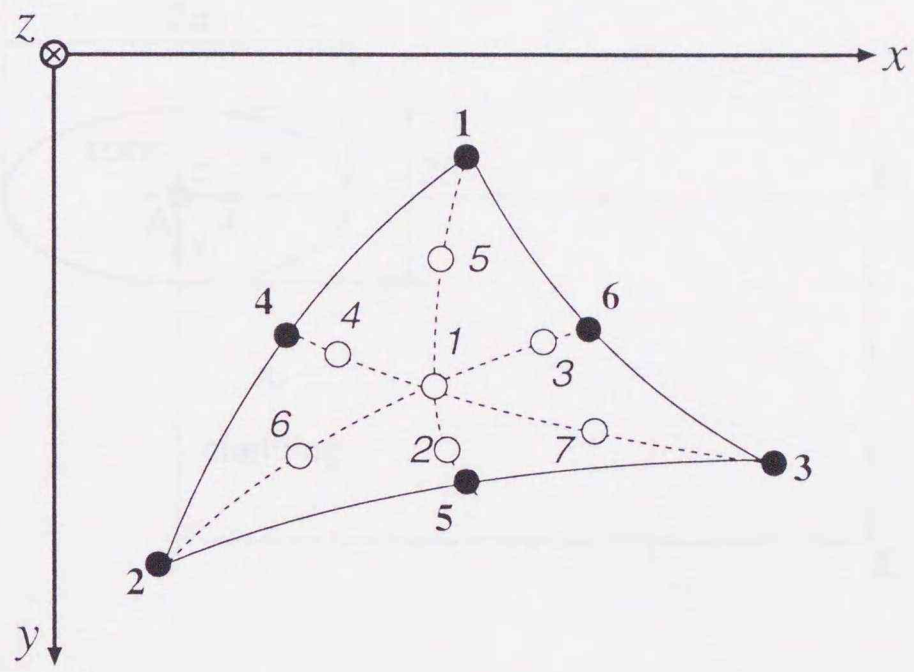

Fig.1 Isoparametric triangular element.

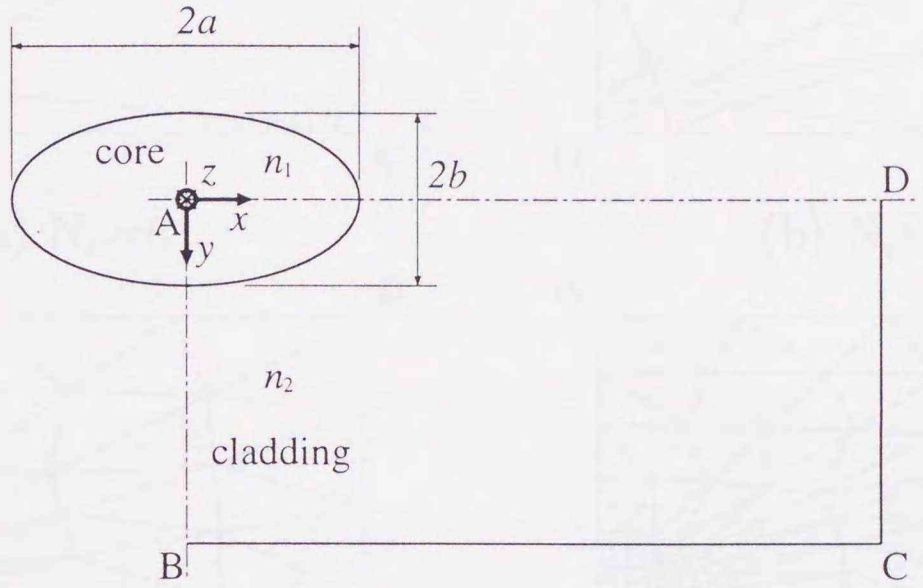

Fig.2 Nonlinear optical elliptical core fiber.

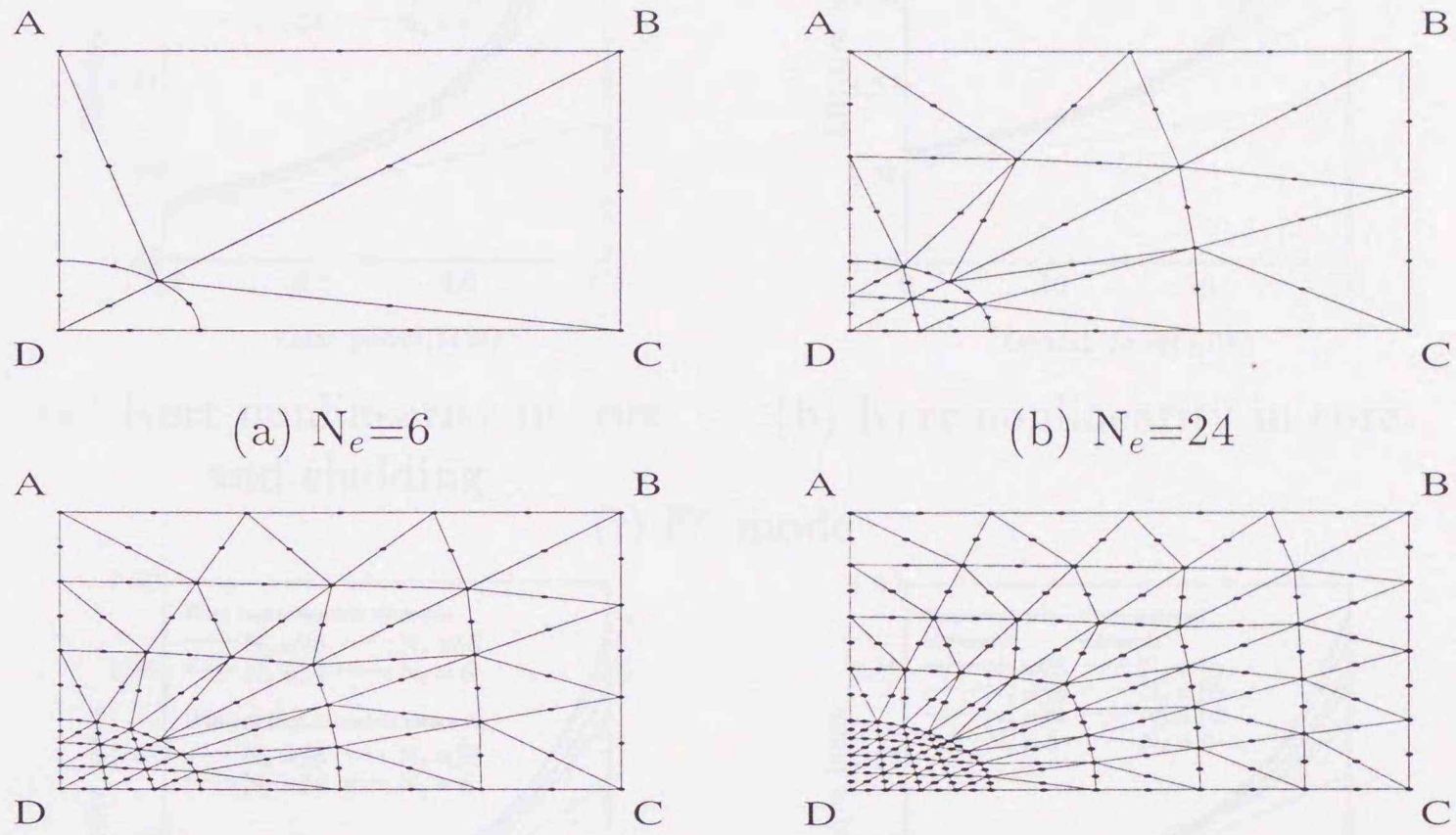

Fig.3 Element divisions for nonlinear optical elliptical core fibers.

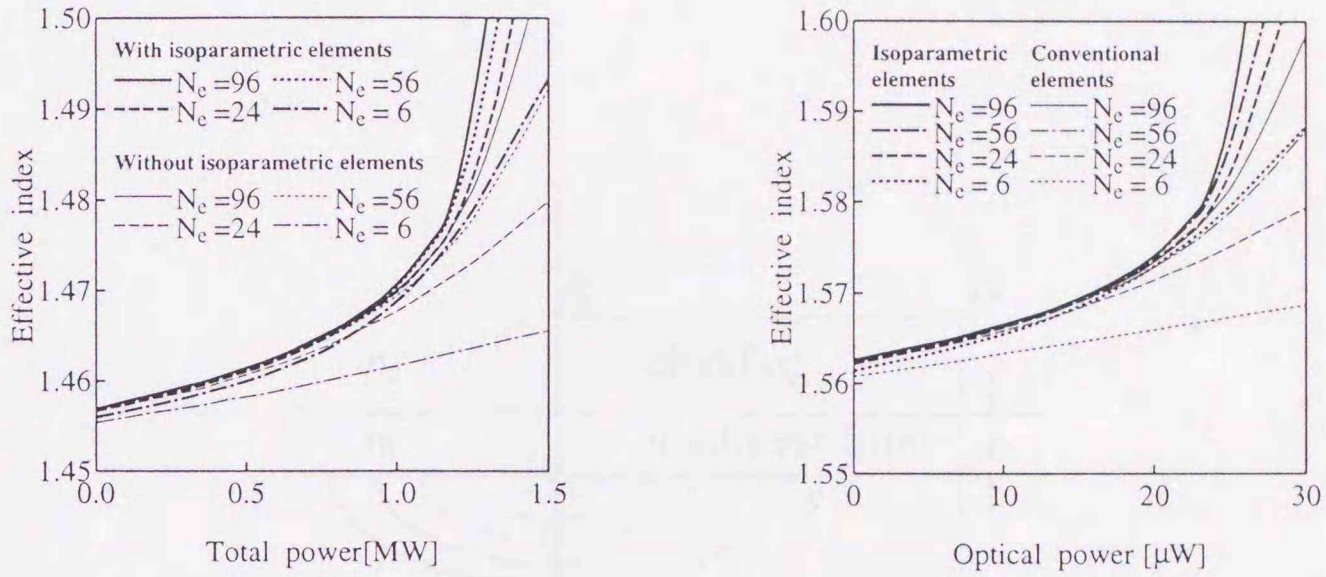

(a) Kerr nonlinearity in core and cladding.

(b) Kerr nonlinearity in core.

(i) E^x mode

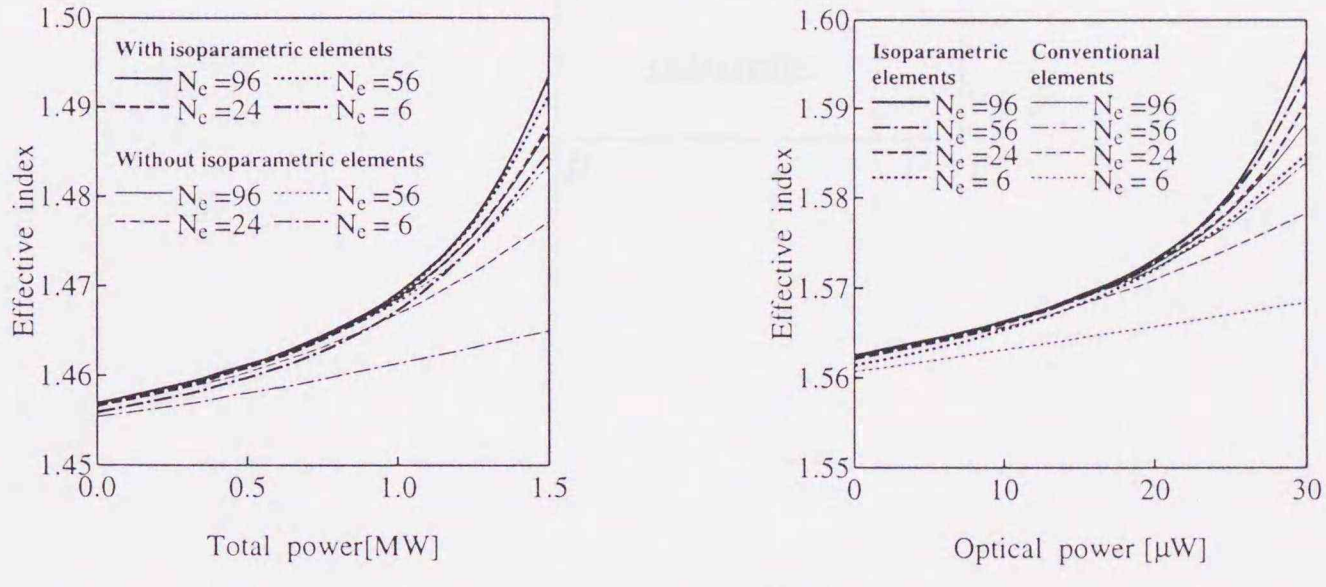

(a) Kerr nonlinearity in core and cladding.

(b) Kerr nonlinearity in core.

(ii) E^y mode

Fig.4 Dependence of optical power on effective indices of nonlinear optical elliptical core fibers.

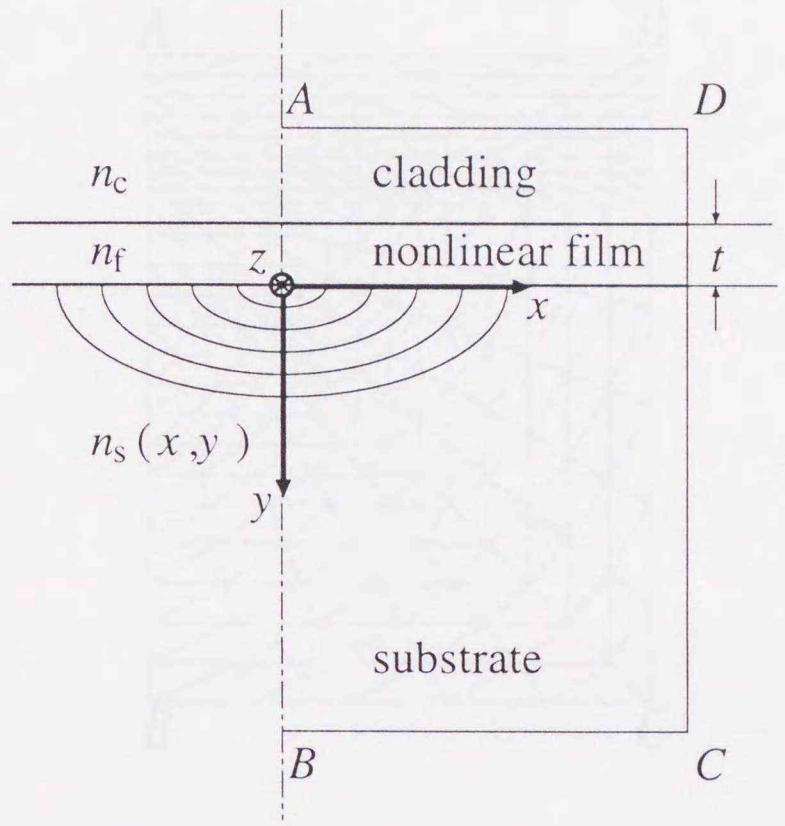

Fig.5 Graded-index nonlinear optical channel waveguide.

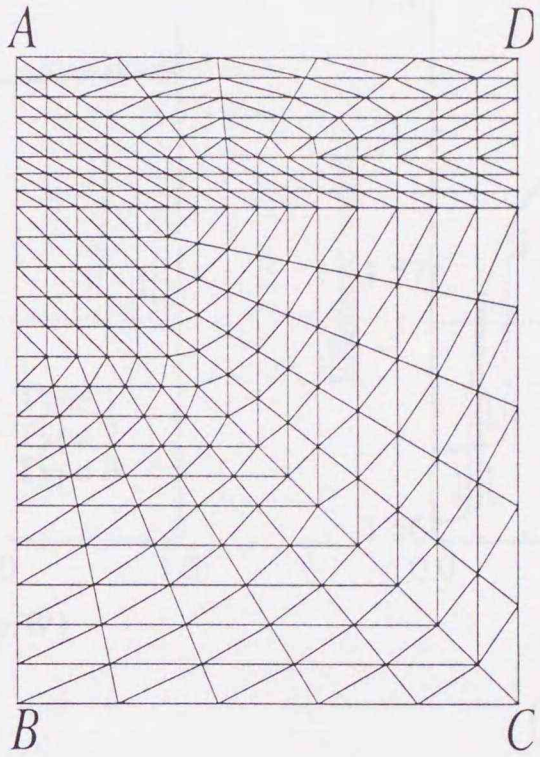

Fig.6 Element division for graded-index nonlinear optical channel waveguides(N_e=440).

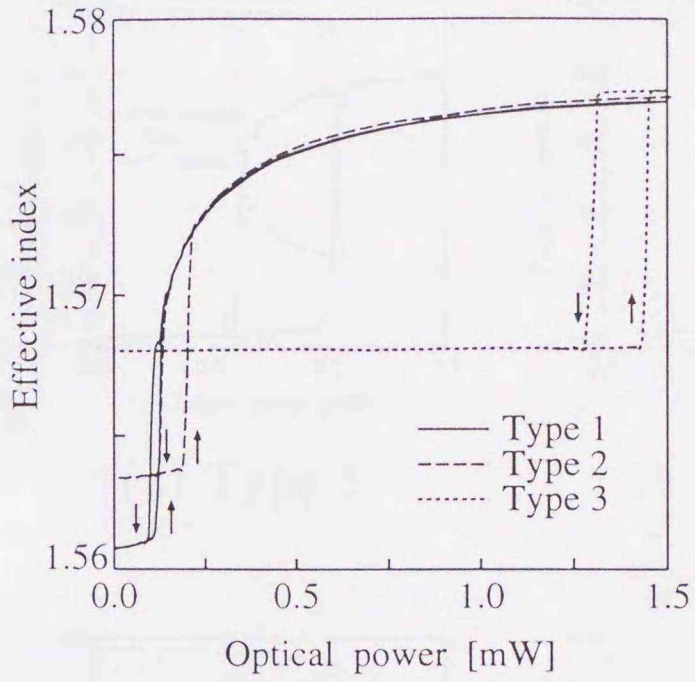

(i) E^x mode

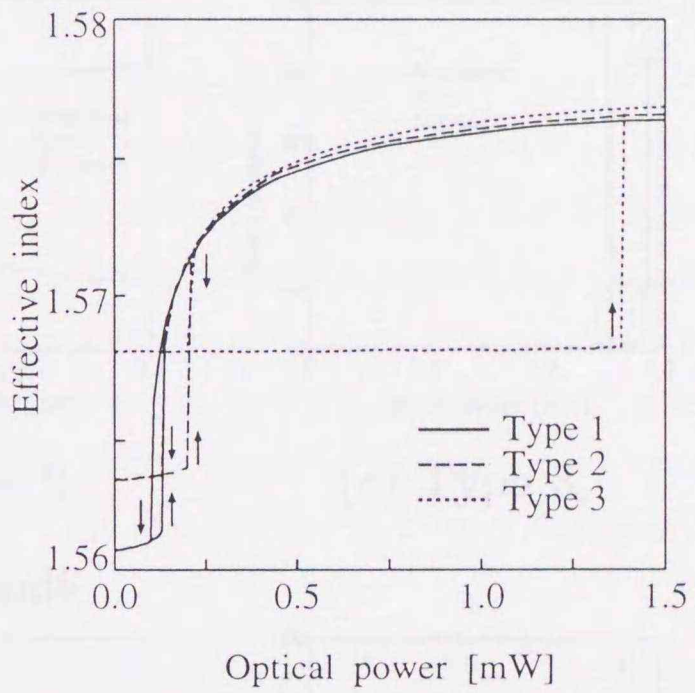

(ii) E^y mode

Fig.7 Dependence of effective indices on optical power.

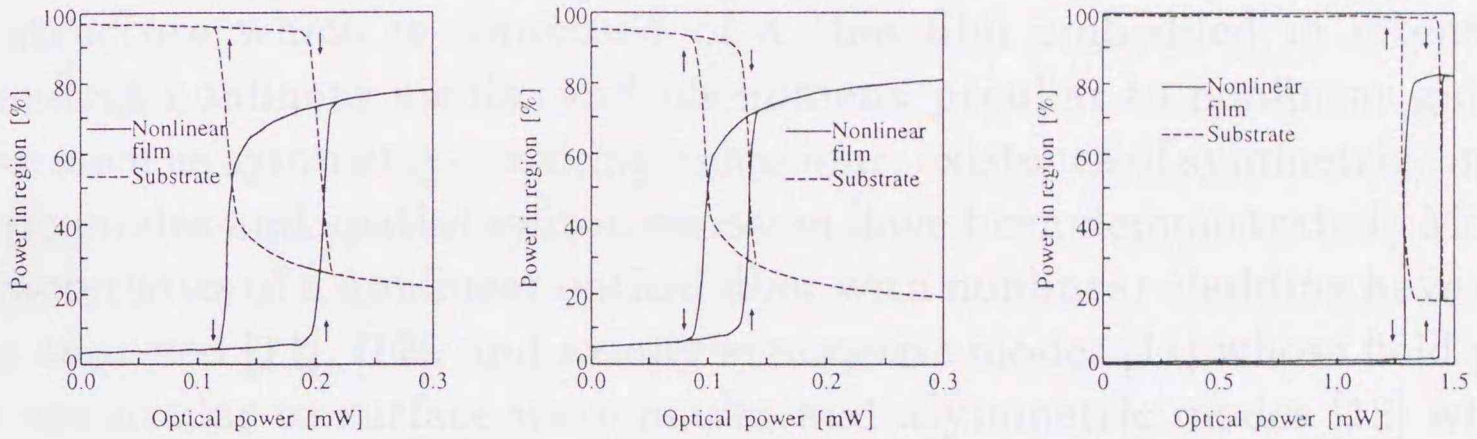

(a) Type 1　(b) Type 2　(c) Type 3

(i) E^x mode

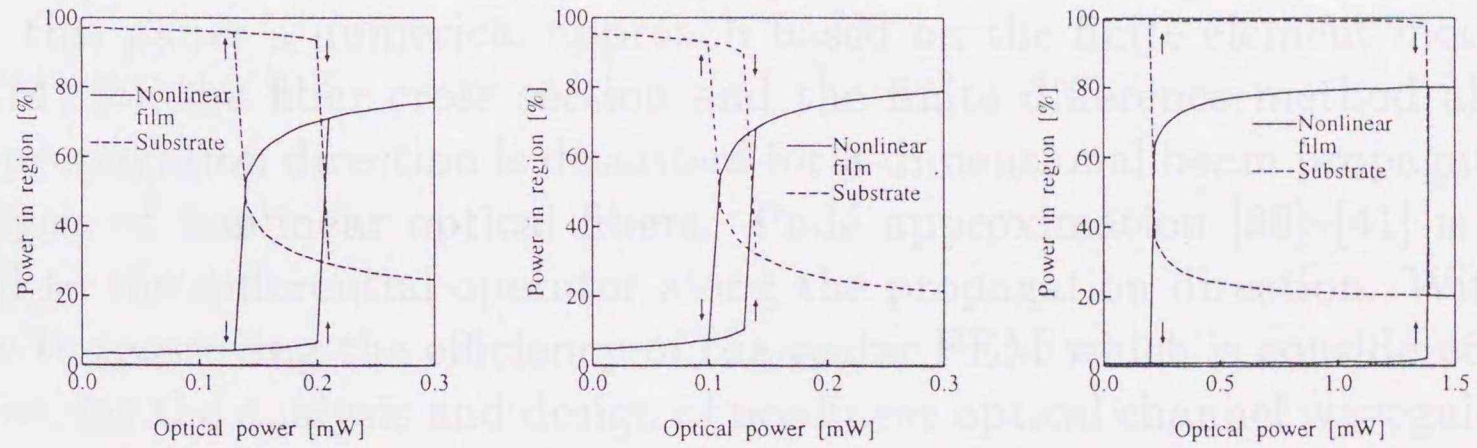

(a) Type 1　(b) Type 2　(c) Type 3

(ii) E^y mode

Fig.8　Optical power distributions.

3 Approximated Scalar Finite Element Beam Propagation Analysis of 3-Dimensional Nonlinear Optical Wavegudes

3.1 Introduction

Recently, modal [9] and/or beam propagation analyses [10] of nonlinear optical waveguides have been performed for a symmetric planar guiding structure which is composed of a thin film embedded in intensity-dependent nonlinear media, and phenomena peculiar to nonlinear guided waves such as symmetry-breaking behaviour, existence of symmetric/ asymmetric modes and spatial soliton emission have been demonstrated. Modal characteristics of a nonlinear optical fiber with nonlinear cladding have also been analyzed [11], [12], and axially symmetric modes [11] whose field profiles are similar to surface wave modes and asymmetric modes [12] whose field profiles have no axial symmetry have been found. To the best of our knowledge, however, the excitation and the stability of these interesting stationary modes have not been investigated.

In this paper a numerical approach based on the finite element method (FEM) for the fiber cross section and the finite difference method along the propagation direction is described for 3-dimensional beam propagation analysis of nonlinear optical fibers. Padé approximation [36]–[41] is applied to the differential operator along the propagation direction. With a view to improving the efficiency of the scalar FEM which is considered effective for the analysis and design of nonlinear optical channel waveguides, isoparametric elements are introduced, and the use of numerical integration formulae derived by Hammer *et al.* [14], [26], [27] is attempted for the calculation of integrals necessary for constructing element matrices. By means of this approach, the refractive index change within each element can be faithfully evaluated according to the electric field distribution without fixing the index constant in each element, and the graded-index nonlinear optical waveguides with curved boundaries can also be easily treated. Using the numerical approach developed here, the modal and propagation characteristics of optical fibers with linear core and nonlinear cladding are analyzed, and the hysteresis nature of the stationary mode, the linear LP_{01} mode excitation and the stability of the stationary mode,

and the spatial soliton emission are investigated. Furthermore, operations of all-optical logic gates using the interaction between optical spatial solitons are investigated. Recently, optical logic gates which consist of a five-layer dielectric structure with a nonlinear layer was proposed [42], and the fundamental and theoretical perspective for realizing all-optical AND, OR, and XOR operations based on the interaction of spatial solitons was investigated. Although the results are very fascinating, because of the difficulty of the broad slab-mode excitation and the self-focusing effect of nonlinear media, the feasibility of these optical logic gates cannot be fully proved with the 2-dimensional analysis. For more practical discussion, it is necessary to deal with 3-dimensional structures. Here, all-optical logic gates with 3-dimensional geometry consisting of optical fibers and a nonlinear film are proposed, and their operations of Boolean arithmetric such as AND, OR, and XOR logic functions are demonstrated.

3.2 Basic Equations

We consider a nonlinear optical fiber with cross section in the xy plane. From Maxwell's equations, the following Helmholtz equation is derived for linearly x-polarized modes with the electric field E_x ($E_y \equiv 0$) as

$$\frac{\partial^2 E_x}{\partial x^2} + \frac{\partial^2 E_x}{\partial y^2} + \frac{\partial^2 E_x}{\partial z^2} + k_0^2 n^2 E_x = 0 \tag{27}$$

where k_0 is the free space wavenumber, and the intensity-dependent refractive index n is given by

$$n = n(x, y, z\ ;\ |\boldsymbol{E}|^2) \tag{28}$$

with $\boldsymbol{E}$ being the electric field vector.

The Helmholtz equation (27) is transformed with the substitution of a solution of the form under the slowly varying envelope approximation (SVEA)

$$E_x(x, y, z) = \phi(x, y, z)\exp(-jk_0 n_0 z) \tag{29}$$

into the following equation for the slowly varying complex amplitude ϕ:

$$\frac{\partial^2 \phi}{\partial z^2} - 2jk_0 n_0 \frac{\partial \phi}{\partial z} + \frac{\partial^2 \phi}{\partial x^2} + \frac{\partial^2 \phi}{\partial y^2} + k_0^2(n^2 - n_0^2)\phi = 0 \tag{30}$$

where n_0 is the reference refractive index.

The electric field vector $\boldsymbol{E}$ used in (28) is approximated as

$$\begin{aligned}\boldsymbol{E}(x,y,z) = \phi &\exp(-jk_0n_0z)\boldsymbol{i}_x \\ &-j(\phi'/k_0n_0)\exp(-jk_0n_0z)\boldsymbol{i}_z \end{aligned} \tag{31}$$

where $\phi' = \partial\phi/\partial x$, $\boldsymbol{i}_x$ and $\boldsymbol{i}_z$ are the unit vectors in the x and z directions, respectively.

3.3 Finite Element Discretization

Dividing the fiber cross section into a number of isoparametric triangular elements [14], [26], [27], and applying the finite element technique to (30), we obtain

$$\begin{aligned}&[M]\frac{d^2\{\phi\}}{dz^2} - 2jk_0n_0[M]\frac{d\{\phi\}}{dz} \\ &+([K(\phi)] - k_0^2n_0^2[M])\{\phi\} + [K]_\Gamma\{\phi\} = \{0\}\end{aligned} \tag{32}$$

with

$$\begin{aligned}[K(\phi)] = \sum_e \iint_e [k_0^2n_e^2(x,y,z;\phi,\phi')\{N\}\{N\}^T \\ -\{N_x\}\{N_x\}^T - \{N_y\}\{N_y\}^T]dxdy \end{aligned} \tag{33}$$

$$[M] = \sum_e \iint_e \{N\}\{N\}^T dxdy \tag{34}$$

$$[K]_\Gamma = \sum_e{}' \int_\Gamma -jk_n\{N\}_\Gamma\{N\}_\Gamma^T d\Gamma \tag{35}$$

where the components of the $\{\phi\}$ vector are the values of ϕ at all nodal points, $\{N\}$ is the shape function vector, $\{N\}_\Gamma$ is the shape function vector on the computational window edge Γ, $\{0\}$ is a null vector, $\{N_x\} \equiv \partial\{N\}/\partial x$, $\{N_y\} \equiv \partial\{N\}/\partial y$, T denotes a transpose, and $\sum_e$ and $\sum_e{}'$ extend over all different elements and the elements related to the boundary Γ, respectively. The parameter k_n included in the matrix $[K]_\Gamma$ is the wavenumber of the outgoing plane wave from the boundary Γ [39]–[43]. The integrants in (33) to (35) are given as the functions of the area coordinates, and thus, the numerical integration formulae derived by Hammer *et al.* [14], [26], [27] can be directly applied. The integral calculations needed

for constructing the matrices $[K(\phi)]$, $[M]$, and $[K]_\Gamma$ can be replaced with simple product-sum calculations [14].

Equation (32) can be rewritten formally as

$$-2jk_0n_0[M]\frac{d\{\phi\}}{dz} = -\frac{([\widetilde{K}(\phi)] - k_0^2n_0^2[M])\{\phi\}}{1 - \frac{1}{2jk_0n_0}\frac{d}{dz}} \tag{36}$$

with

$$[\widetilde{K}(\phi)] = [K(\phi)] + [K]_\Gamma \tag{37}$$

Utilizing Padé approximation [36]–[41] and replacing d/dz in the denominator of (36) by

$$\frac{d}{dz} \simeq \frac{1}{2jk_0n_0}[M]^{-1}([\widetilde{K}(\phi)] - k_0^2n_0^2[M]) \tag{38}$$

the following Padé equation is obtained:

$$\begin{aligned} &-2jk_0n_0[\widetilde{M}(\phi)]\frac{d\{\phi\}}{dz} \\ &+([\widetilde{K}(\phi)] - k_0^2n_0^2[M])\{\phi\} = \{0\} \end{aligned} \tag{39}$$

with

$$[\widetilde{M}(\phi)] = [M] + \frac{1}{4k_0^2n_0^2}([\widetilde{K}(\phi)] - k_0^2n_0^2[M]) \tag{40}$$

The Fresnel or paraxial equation is easily obtained from (39) by replacing the matrix $[\widetilde{M}(\phi)]$ by $[M]$.

3.4 Crank-Nicholson Algorithm

Applying the Crank-Nicholson algorithm for the propagation direction, z, to (39) yields

$$[A(\phi)]_i\{\phi\}_{i+1} = [B(\phi)]_i\{\phi\}_i \tag{41}$$

with

$$\begin{aligned} [A(\phi)]_i = &-2jk_0n_{0,i}[\widetilde{M}(\phi)]_i \\ &+0.5\Delta z([\widetilde{K}(\phi)]_i - k_0^2n_{0,i}^2[M]_i) \end{aligned} \tag{42}$$

$$\begin{aligned} [B(\phi)]_i = &-2jk_0n_{0,i}[\widetilde{M}(\phi)]_i \\ &-0.5\Delta z([\widetilde{K}(\phi)]_i - k_0^2n_{0,i}^2[M]_i) \end{aligned} \tag{43}$$

where Δz is the propagation step size, and the subscripts i and $i+1$ denote the quantities related to the ith and $(i+1)$th propagation steps, respectively.

The reference refractive index n_0 is renewed at each propagation step automatically as [39]–[41], [44]

$$n_{0,i}^2 = \mathrm{Re}\left[\frac{\{\phi\}_i^\dagger [\widetilde{K}(\phi)]_i \{\phi\}_i}{k_0^2 \{\phi\}_i^\dagger [M]_i \{\phi\}_i}\right] \tag{44}$$

where $\dagger$ denotes complex conjugate and transpose.

Equation (41) can be solved with the following iterative scheme:

1) Specify the refractive index n, the wavelength $\lambda = 2\pi/k_0$, and optical power as input data.

2) Assign initial values of the reference refractive index n_0 and the slowly varying complex amplitude $\{\phi\}$.

3) Calculate coefficient matrices $[A]$ and $[B]$ and solve (41) for a new solution $\{\phi\}_{i+1}$.

4) Update n from (28) and n_0 from (44).

5) Iterate the above procedure 2), 3), and 4) until we reach the desired number of iterations in the z direction.

3.5 Numerical Results and Discussion

3.5.1 Modal Analysis of Nonlinear Optical Fiber

The modal analysis [14] can be easily performed by setting $d/dz = 0$ in (32), and then n_0 becomes the modal effective index, n_{eff}, and $\{\phi\}$ is the corresponding modal (stationary) field. An iterative scheme for solving this nonlinear generalized eigenvalue problem has already been reported in [14]. We consider a nonlinear optical fiber as shown in Fig. 9. Here, we subdivide all the fiber cross section into 360 isoparametric elements, and the Neumann condition ($\partial\phi/\partial n = 0$ with $\partial/\partial n$ being the outward normal derivative) is imposed on all the computational window edges.

Fig. 10 shows power dispersion curves for the fundamental (LP_{01}) mode of a nonlinear optical fiber with saturable nonlinearity in the cladding,

where P is the input optical power, the wavelength $\lambda = 1.3\mu$m, the core diameter $a = 5\mu$m, the refractive index of the core $n_1 = 1.57$, and the refractive index of the cladding is given by

$$n_2 = n_L + \Delta n_{sat}\left[1 - \exp\left(-\frac{n_L n'|\boldsymbol{E}|^2}{2Z_0\Delta n_{sat}}\right)\right]$$

Here, the linear part of the nonlinear refractive index $n_L = 1.55$, the nonlinear optical coefficient $n' = 10^{-9}\text{m}^2/\text{W}$, the saturation of the nonlinearity $\Delta n_{sat} = 0.04$, and Z_0 is the free space impedance.

The change in the effective index with optical power is initially slower, but above a certain threshold the symmetry of the mode is broken and the field is localized near the core-cladding boundary in nonlinear cladding, causing a jump in the effective index. When decreasing optical power, the dispersion curve exhibits hysteresis nature and the mode returns abruptly to the linear core.

Figure 11 shows the field distributions at $P = 0.5$mW and 5.5mW. When optical power is below the threshold, most of the power is within the core region, but when optical power increases beyond the threshold, the symmetry-breaking behaviour is observed, suddenly most of the power moves to the cladding, the power inside the core falls drastically, and the field becomes axially asymmetric.

3.5.2 Beam Propagation Analysis of Nonlinear Optical Fiber

We consider a nonlinear optical fiber with saturable nonlinearity in the cladding and make an attempt to estimate the behaviour of propagating waves excited by launching the linear LP_{01} mode. The analysis condition is the same as in the modal analysis, except that the transparent boundary condition is imposed on all the computational window edges.

Figure 12 shows the contour plots of field amplitudes, where the input LP_{01} power $P = 0.5$mW. Since this low input power does not stimulate the cladding nonlinearity, the excited beam is propagating stably up to the distance $l = 200\mu$m, and the beam profile is quite similar to that of the linear LP_{01} field. Figure 13 also shows the contour plots for $P = 5.5$mW. This input power is enough to stimulate the cladding nonlinearity and to break the power confinement. At the propagation distance $l \simeq$

30 to 70μm, a ring-shaped beam surrounding the core is formed, and the intensity maxima lie near the core-cladding boundary in nonlinear cladding. The shape is quite similar to the ring-shaped surface mode found by assuming axially symmetric solutions [11]. The axially symmetric ring mode is unstable, the symmetry is broken at $l \simeq 70$ to 80μm, and the beam splits into two packets. Then, these two beams draw each other, and coalesce in the core region, but repulse each other again, and finally are emitted into the cladding region. These emitted beams behave themselves like spatial solitons [10], and may be applicable for constructing active optical devices such as soliton couplers [45] and optical logic gates [42].

3.5.3 All-Optical Logic Gates

As all-optical logic gates with 3-dimensional structure, we consider a waveguide-type nonlinear optical device as shown in Fig. 14, where the wavelength $\lambda = 1.064\mu$m, the core diameter $a = 2\mu$m, the refractive indices of core and cladding $n_1 = 1.57$ and $n_2 = 1.55$, respectively, the nonlinear film thickness $t = 3\mu$m, and the refractive index of the nonlinear film is given by

$$n_3 = n_L + \Delta n_{sat}\left[1 - \exp\left(\frac{-n_L n' |\boldsymbol{E}|^2}{2Z_0 \Delta n_{sat}}\right)\right]$$

Here, the linear part of the nonlinear refractive index $n_L = 1.55$, the nonlinear optical coefficient $n' = 10^{-9}\mathrm{m}^2/\mathrm{W}$, the saturation of the nonlinearity $\Delta n_{sat} = 0.04$, and Z_0 is the free space impedance.

We assume the device input by launching the linear LP_{01} mode into the left and right cores, that is, input ports, and the output by detecting the optical power in the nonlinear film, that is, output port. At first, we should define the correlation between propagating beams and binary state in the optical logic gate. The Boolean logic state in the device considered here is related to the existence of optical power in the ports, in other words, the presence/absence of power in each port represents the Boolean variable such as "1/0", "H/L", or "T/F". The output Boolean variable can be decided by comparing the output power to certain threshold.

In our binary criterion, the output state is set to "1" if the output power in the nonlinear film occupies over 50% of the input power per port P,

and is set to "0" otherwise. For the sake of simplicity and convenience, we introduce the concept of the input power per port P to the expression of the launching power. In short, $P = P_{in}$ for single-port excitation and $P = P_{in}/2$ for double-port excitation, where P_{in} represents total input power.

The device length is determined so that spatial soliton interactions in the device can realize the operation of Boolean logic functions. Figure 15 shows the condition of input-port excitation and device length for the power emergence in the output port which satisfies our binary criterion for setting the variable "1". The region with horizontal lines denotes the possible region to define the output as "1" for single-port excitation, and the region with vertical lines also denotes the same region but for double-port excitation, without relative phase difference. The darkest area is the overlap of them. From this figure we can get the information how to choose the input power and the device length in order to realize desired Boolean AND/OR functions. In addition, if we consider the case of double-port excitation with relative phase difference of π, output port is set to "0" in the region of $P < 250\mu$W and the device length shorter than 150μm. Therefore, we can also realize the XOR function by using the combination of single-port and double-port opposite-phase excitations.

Figure 16 shows an example of AND gate operation with $P = 150\mu$W. In the case of single-port excitation, the launching LP_{01} beam is propagating stably up to 70μm, and the beam profile is remaining as the LP_{01} mode. The input power is not so high for spatial soliton emission, except for double-port in-phase excitation at the same P. A couple of LP_{01} incident beams stimulates the film nonlinearity, and allows spatial solitons to emit. At the propagation distance $l \simeq 40\mu$m, the two beams are coupled, and most of the power is shifted to the nonlinear film at $l = 70\mu$m. In our binary criterion, output port is set to "0" in single-port excitation and "1" in double-port excitation, and considering the state of input and output ports in our binary criterion, this optical logic gate acts as AND gate, that is "$0 \wedge 1 = 1 \wedge 0 = 0$" in single-port excitation and "$1 \wedge 1 = 1$" in double-port excitation. The result "$0 \wedge 0 = 0$" is trivial, taking the situation that no beam excitation makes no output into account.

Figure 17 shows an example of OR gate operation with higher input power $P = 250\mu$W than that in the AND gate example. The input power

is high enough to emit the spatial soliton in single-port excitation. The excited beam in the output port is moving to the nonlinear film in the 70μm propagation. In double-port in-phase excitation at the same P, the two beams are coupled at $l \simeq 30\mu$m, most of the power lies in the nonlinear film at $l \simeq 40\mu$m to 70μm. Considering the state of input and output ports in our binary criterion, this optical logic gate acts as OR gate, that is, "$0 \vee 1 = 1 \vee 0 = 0$" in single-port excitation, "$1 \vee 1 = 1$" in double-port excitation, and the trivial result of "$0 \vee 0 = 0$".

Figure 18 shows an example of XOR gate operation with $P = 250\mu$W. The result of single-port excitation is the same as the OR gate example in Fig. 17(a), and most of the power lies in the nonlinear film at $l = 100\mu$m. As mentioned above, the XOR function can be realized by using the combination of single port and double-port opposite-phase excitations. In double-port opposite-phase excitation, the film nonlinearity is not so stimulated as the in-phase excitation case, because of the cancellation of electric field near the core-film interface, and the zero-intensity distribution is remaining up to 100μm in the nonlinear film. In the same way as the AND and OR gate examples, considering the binary state of input and output ports in our binary criterion, the XOR logic function can be proved as "$0 \oplus 1 = 1 \oplus 0 = 0$" in single-port excitation, "$1 \oplus 1 = 1$" in double-port excitation, and the trivial result of "$0 \oplus 0 = 0$".

These results show that AND, OR, and XOR logic gates are feasible without changing the transverse structure, but we should choose suitable input power, relative phase of double-port excitation, and device length for each logic gate to link the spatial-soliton interaction with logic functions.

3.6 Conclusion

We have newly formulated an efficient 3-dimensional beam-propagation approach based on the Crank-Nicholson finite element method for the analysis of nonlinear optical fibers. Using the numerical approach developed here, both the modal and propagation characteristics of optical fibers with linear core and nonlinear cladding have been analyzed. We have confirmed the existence of the symmetric and asymmetric stationary modes. When launching the linear LP_{01} mode with relatively high power onto the fiber center, the spatial soliton emission has been observed. Furthermore,

all-optical logic gates with practical, 3-dimensional geometry consisting of optical fibers and a nonlinear film have been proposed, and their operations of Boolean arithmetric have been demonstrated.

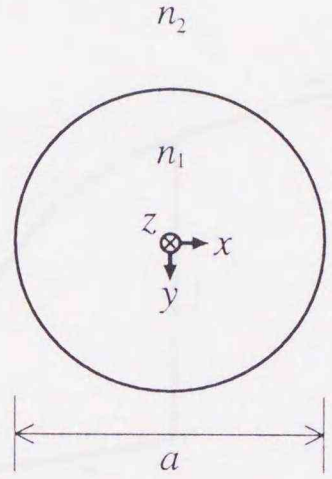

Fig. 9 Nonlinear optical fiber.

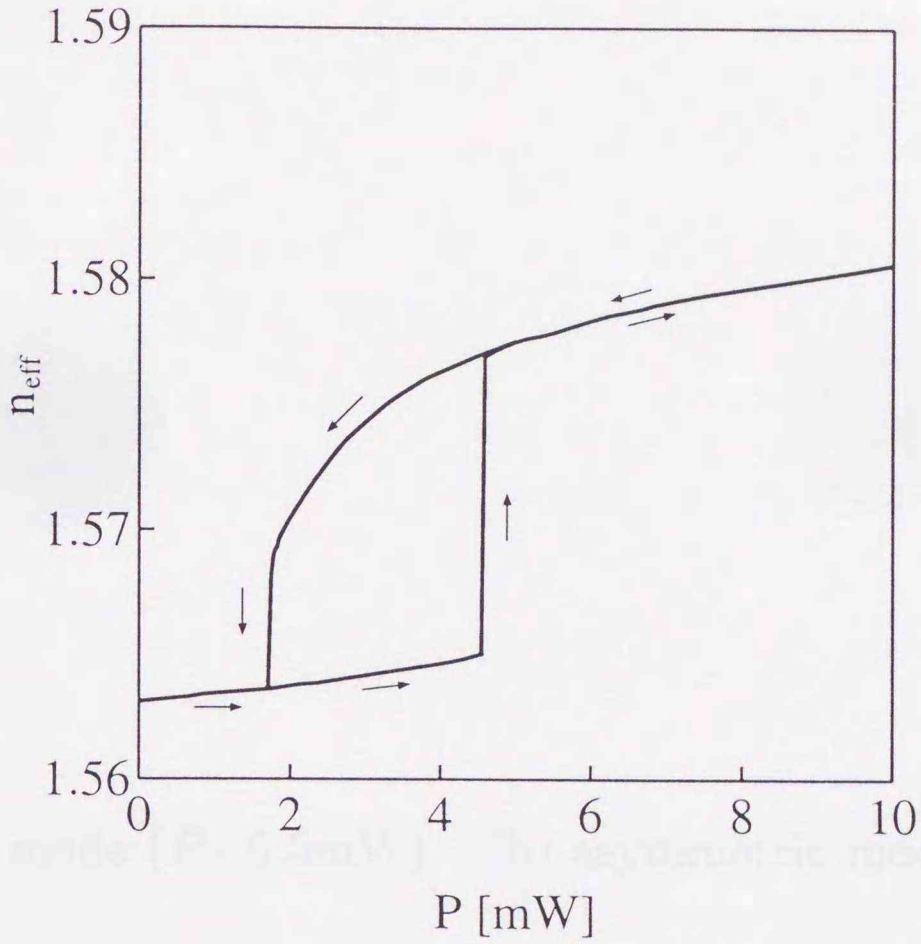

Fig. 10 Power dispersion curves for the fundamental (LP_{01}) mode of a nonlinear optical fiber with saturable nonlinearity in the cladding.

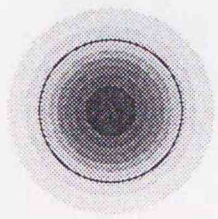

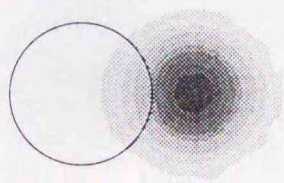

(a) symmetric mode (P=0.5mW). (b) asymmetric mode (P=5.5mW).

Fig. 11 Optical field distributions.

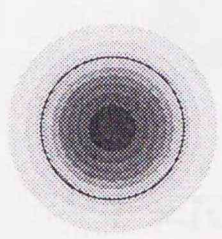

(a) input beam.

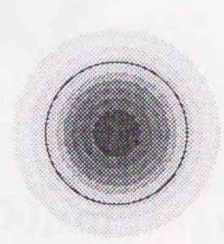

(b) $l = 200\mu$m.

Fig. 12 Contour plots of propagating waves excited by the LP_{01} mode (P=0.5mW).

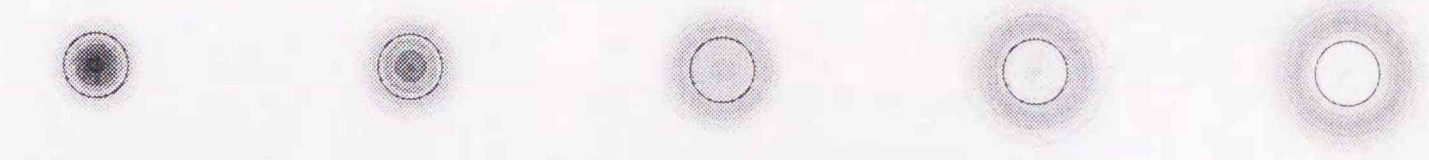

l =10μm l =20μm l =30μm l =40μm l =50μm

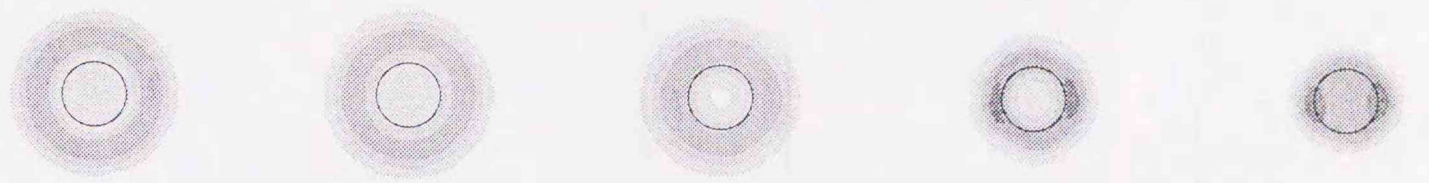

l =60μm l =70μm l =80μm l =90μm l =100μm

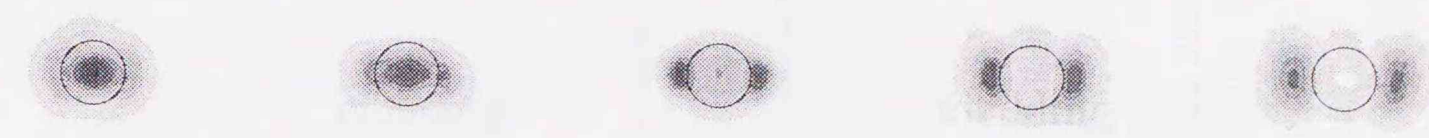

l =110μm l =120μm l =130μm l =140μm l =150μm

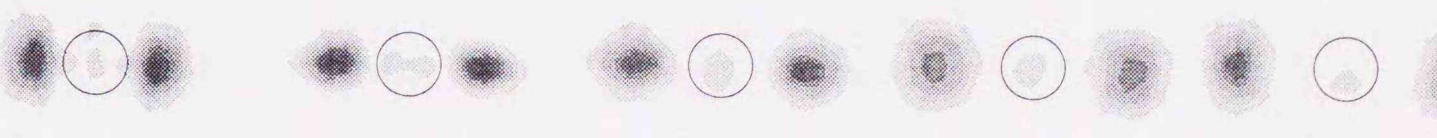

l =160μm l =170μm l =180μm l =190μm l =200μm

Fig. 13 Contour plots of propagating waves excited by the LP_{01} mode (P=5.5mW).

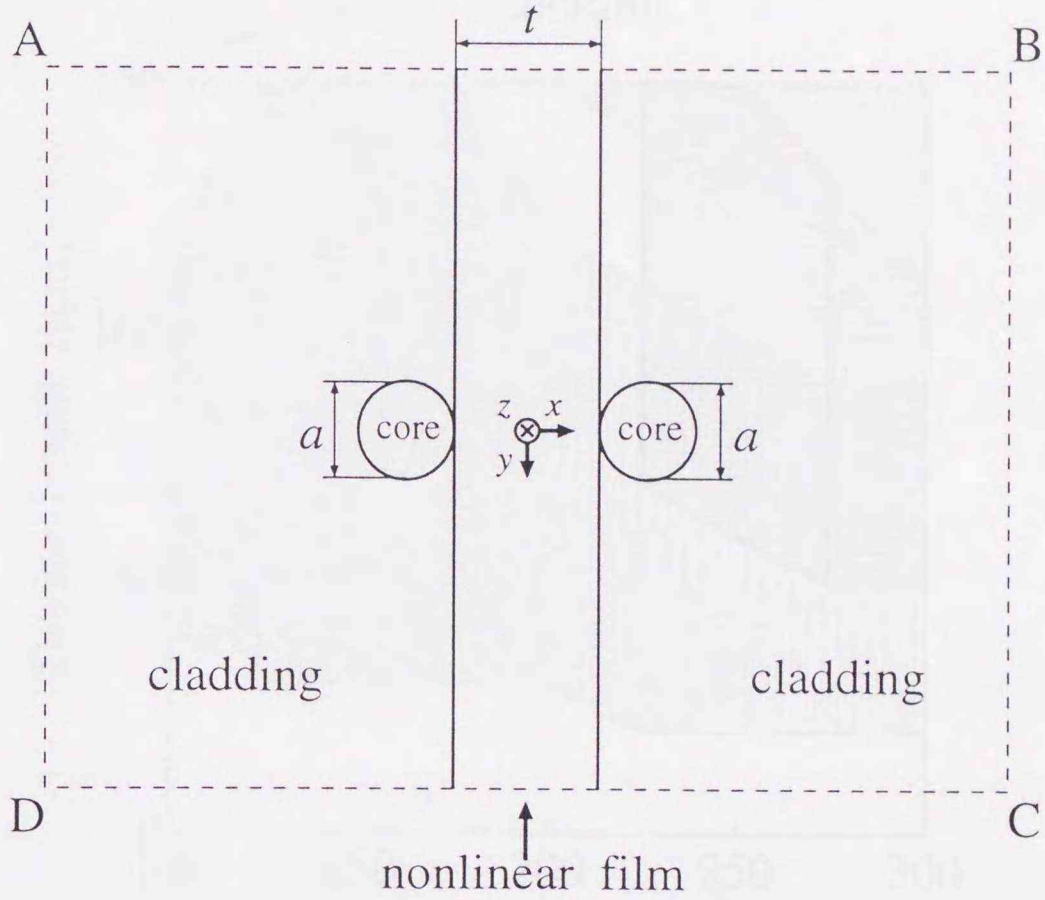

Fig. 14 Optical logic gate.

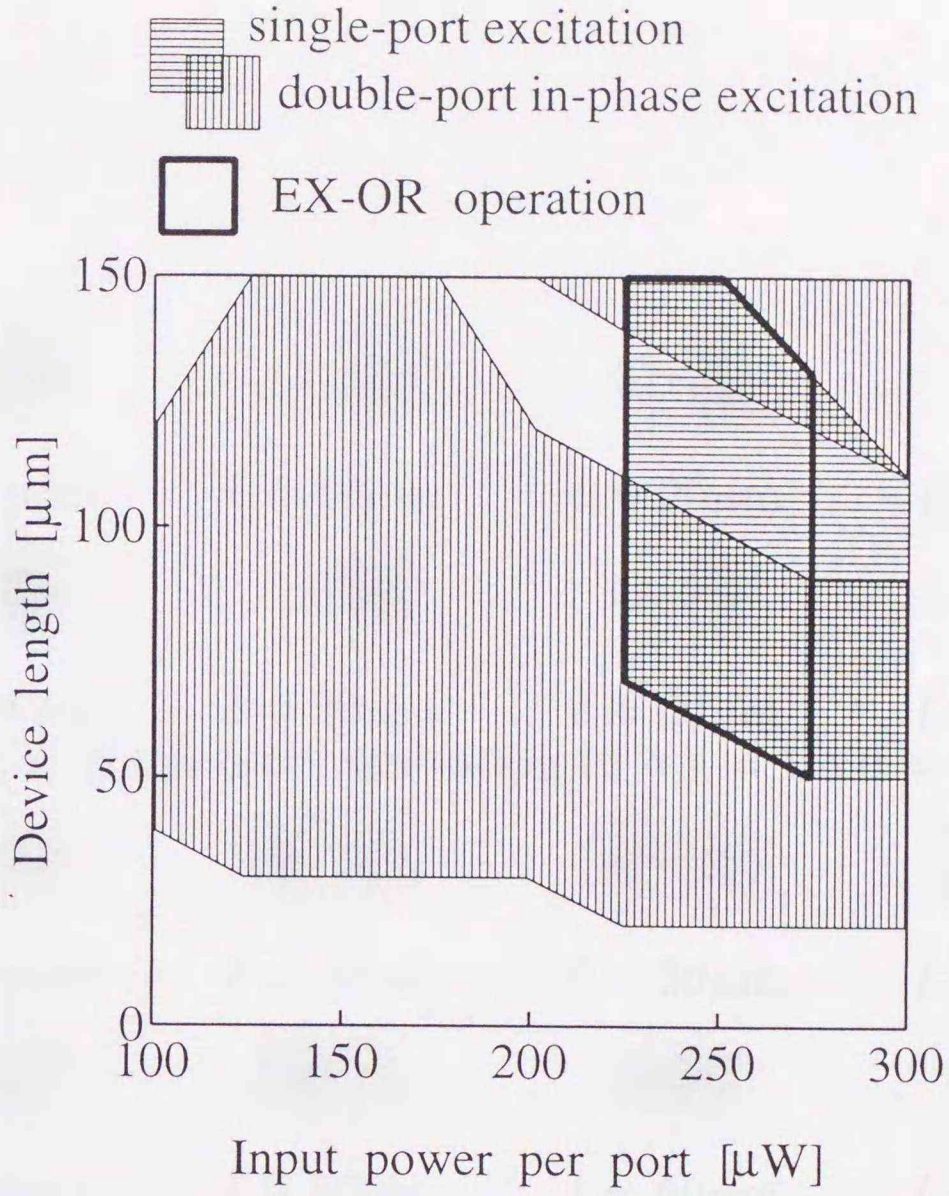

Fig. 15 Regions of acceptable input power and device length corresponding to the binary variable of "1".

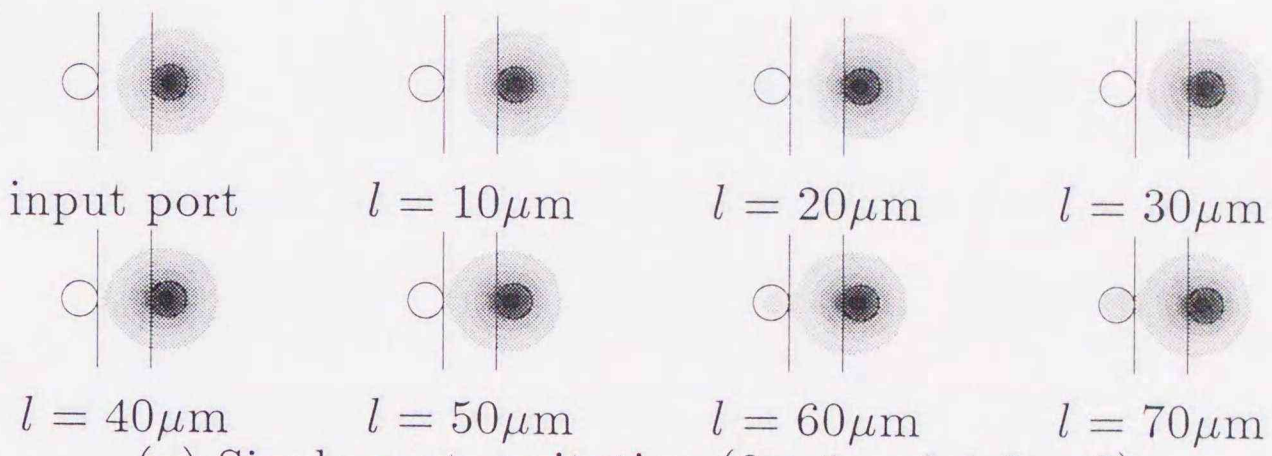

(a) Single-port excitation ($0 \wedge 1 = 1 \wedge 0 = 0$).

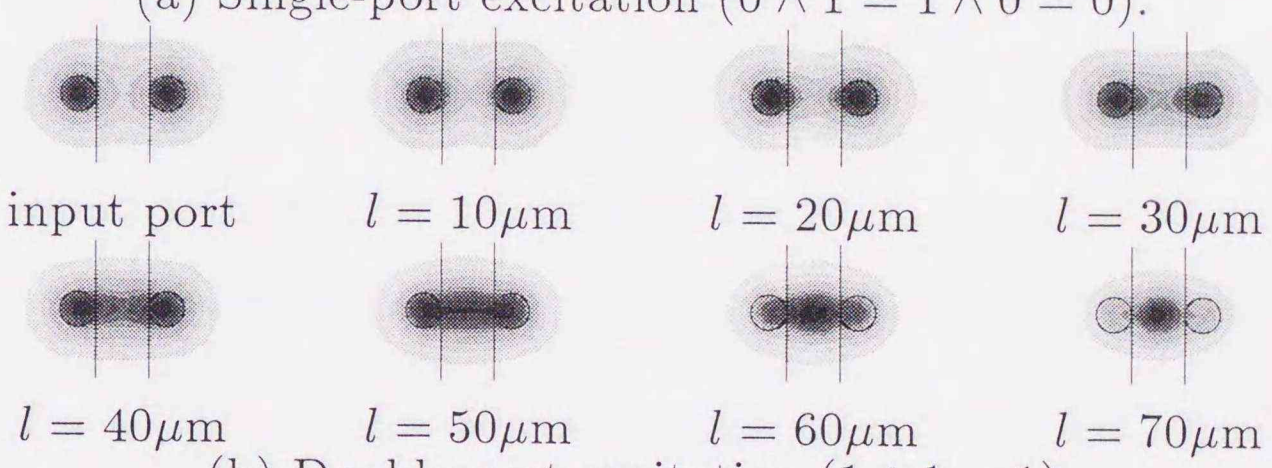

(b) Double-port excitation ($1 \wedge 1 = 1$).

Fig. 16 AND logic function ($P = 150\mu$m).

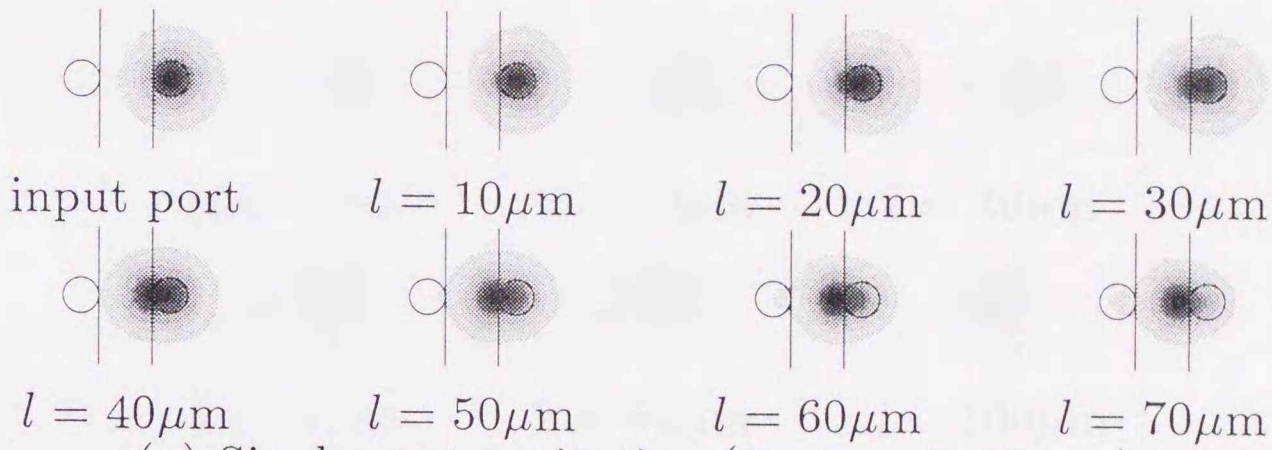

(a) Single-port excitation ($0 \vee 1 = 1 \vee 0 = 1$).

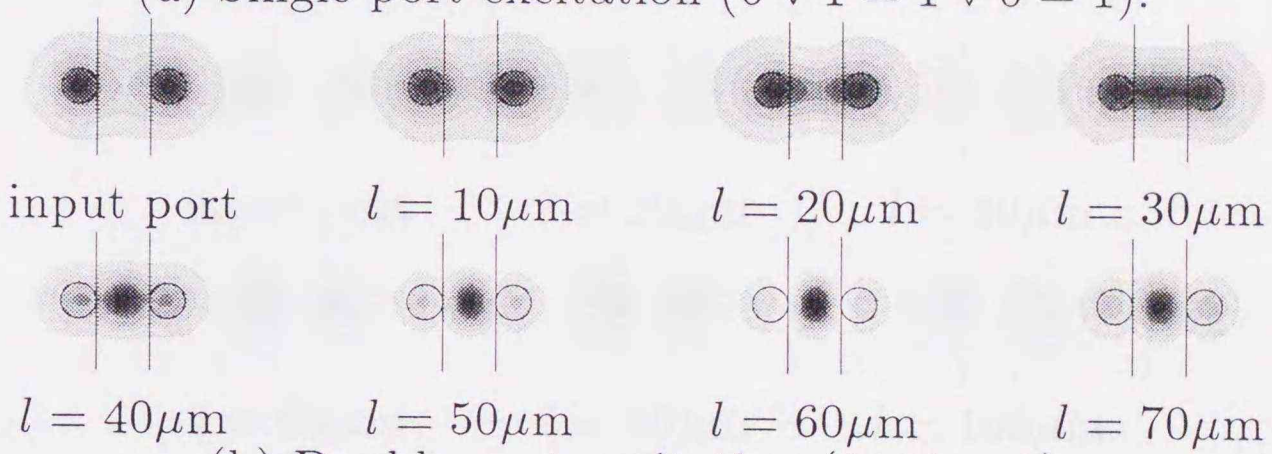

(b) Double-port excitation ($1 \vee 1 = 1$).

Fig. 17 OR logic function ($P = 250\mu$m).

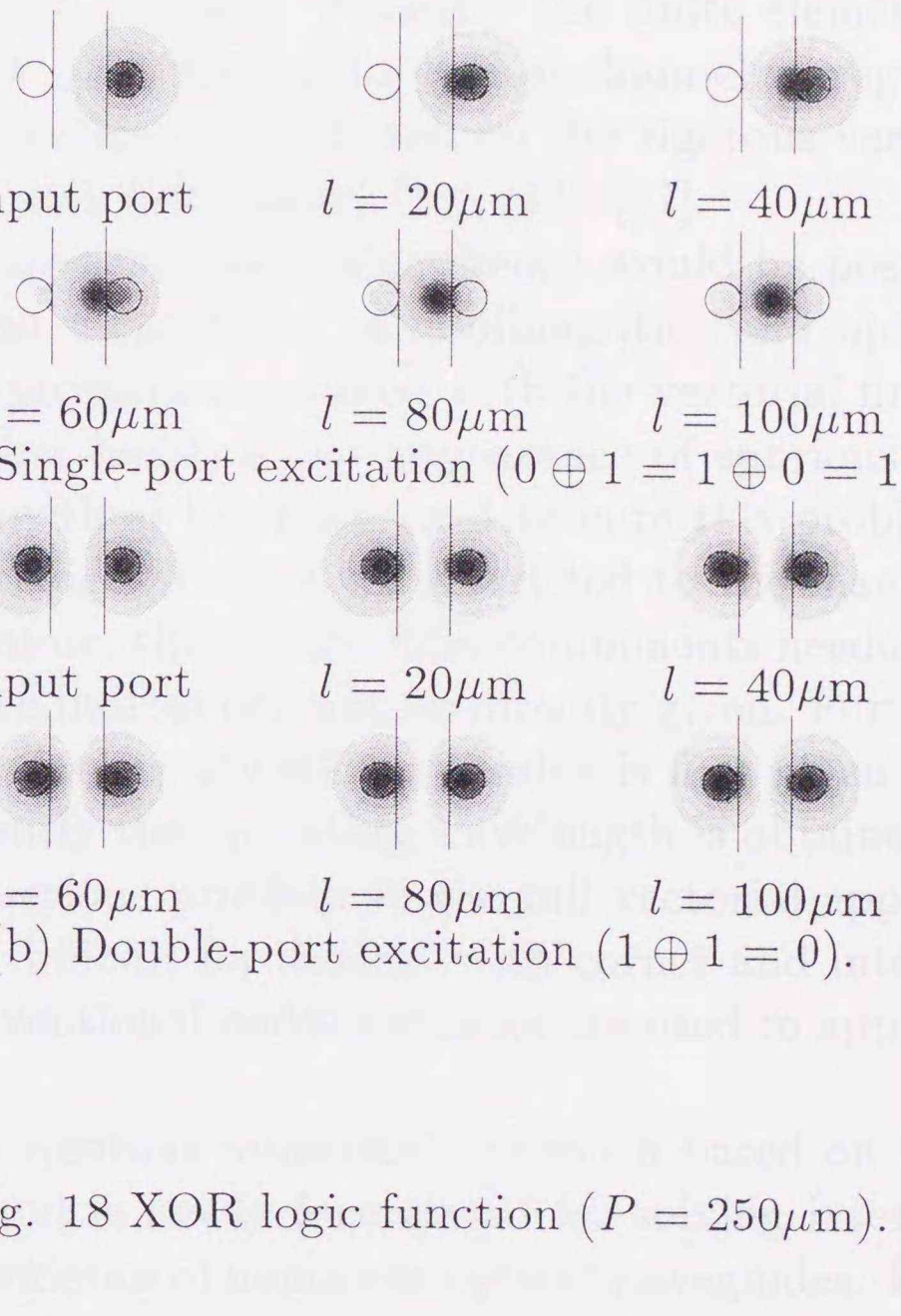

(a) Single-port excitation ($0 \oplus 1 = 1 \oplus 0 = 1$).

(b) Double-port excitation ($1 \oplus 1 = 0$).

Fig. 18 XOR logic function ($P = 250\mu$m).

4 Vector Finite Element Analysis of 3-Dimensional Nonlinear Optical Wavegudes

4.1 Introduction

Nonlinear optical waveguides have many potential applications in all-optical signal-processing devices. For channel waveguides, all six components of electromagnetic field vectors are involved, indicating that full-wave calculations are needed. Recently the finite element method with nodal elements has been applied to optical channel waveguides with Kerr and/or Kerr-like nonlinearities, based on the rigorous vectorial approach [15]–[20], or the scalar field theory [13], [14], [17].

The use of the approximate scalar theory would be possible under certain restrictions on magnitudes of nonlinearities and optical intensities. The most serious problem associated with the vectorial finite element approach, on the other hand, is the appearance of spurious solutions. The penalty function method has been used to cure this problem, but in this technique the working variables are restricted to the magnetic field components, and therefore, the electric field components needed for evaluating nonlinear refractive indices can not be directly given. Furthermore, in the full vectorial formulation, the effective index is first given as an input datum and subsequently the operating wavelength is obtained as a solution. There is another serious problem in the full vectorial approach. Such an approach is quite difficult for dealing with corner and interface singularities so long as conventional nodal elements are used to approximate vector fields.

In this paper, a rigorous numerical approach based on the vectorial finite element method is newly formulated for solving intensity-dependent dispersion characteristics of nonlinear optical waveguides. In order to eliminate spurious solutions and to treat corner and interface singularities, the hybrid element [21], [22] is introduced. It is a combination of the edge element for transverse components of the electric or magnetic field and the nodal element for the axial one. The present approach can solve directly the effective index and the corresponding field distribution at a given operating wavelength. To confirm the validity of the newly formulated full-wave approach, nonlinear dispersion characteristics are cal-

culated for optical fibers, strip-loaded optical channel waveguides, and multiple-quantum-well-embedded optical channel waveguides. A comparison is made with results computed by a simple scalar finite element method previously developed by the authors. Serious limitations on the validity of the scalar field approximation are found in the high power regime, where nonlinearities are expected to play an essential role in forming the stationary mode.

4.2 Basic Equations

We consider a nonlinear optical waveguide with cross section in the xy plane. From Maxwell's equations, the following vectorial wave equation for the electric field vector $\boldsymbol{E}$ is derived:

$$\nabla \times \nabla \times \boldsymbol{E} - k_0^2 n^2 \boldsymbol{E} = 0 \tag{45}$$

where k_0 is the free space wavenumber and n is the intensity-dependent nonlinear refractive index expressed as

$$n = n(x, y\ ;\ |\boldsymbol{E}|^2). \tag{46}$$

The functional for this wave equation is given by

$$F = \iint_\Omega [(\nabla \times \boldsymbol{E})^* \cdot (\nabla \times \boldsymbol{E}) - k_0^2 n^2 \boldsymbol{E}^* \cdot \boldsymbol{E}] dx dy \tag{47}$$

where $*$ denotes complex conjugate.

4.3 Finite Element Discretization

Dividing the waveguide cross section into a number of high-order hybrid edge/nodal triangular elements [21], [22] as shown in Fig. 19, the electric field vector $\boldsymbol{E}$ in each element is expressed as

$$\boldsymbol{E} = \begin{bmatrix} E_x \\ E_y \\ E_z \end{bmatrix} = \begin{bmatrix} \{U\}^T \{E_t\}_e \\ \{V\}^T \{E_t\}_e \\ j\{N\}^T \{E_z\}_e \end{bmatrix} \tag{48}$$

where $\{U\}$ and $\{V\}$ are the shape function vectors for the linear edge element, $\{N\}$ is the ordinary shape function vector for the quadratic nodal

element, T denotes a transpose, $\{E_t\}_e$ is the edge variables in the transverse plane for each element, and $\{E_z\}_e$ is the nodal axial-field vector for each element. More detailed informations about the formulation of the vector finite element method (VFEM) with high-order hybrid edge/nodal triangular elements can be found in [21].

Applying the finite element technique to (60), we obtain the following matrix equation which gives solutions directly for the propagation constant β and the corresponding field distributions:

$$\begin{bmatrix} [K_{tt}] & [0] \\ [0] & [0] \end{bmatrix} \begin{bmatrix} \{E_t\} \\ \beta^{-1}\{E_z\} \end{bmatrix} - \beta^2 \begin{bmatrix} [M_{tt}] & -[K_{tz}] \\ -[K_{zt}] & [K_{zz}] \end{bmatrix} \begin{bmatrix} \{E_t\} \\ \beta^{-1}\{E_z\} \end{bmatrix} = \begin{bmatrix} \{0\} \\ \{0\} \end{bmatrix} \tag{49}$$

with

$$\begin{aligned} [K_{tt}(\boldsymbol{E})] = \sum_e \iint_e \big[& n^2 k_0^2 (\{U\}\{U\}^T \\ & + \{V\}\{V\}^T) \\ & + (\{U_y\} - \{V_x\}) \\ & \times (\{V_x\}^T - \{U_y\}^T)\big]\, dxdy \end{aligned} \tag{50}$$

$$\begin{aligned} [K_{tz}] = \sum_e \iint_e \big[& (\{U\}\{N_x\}^T \\ & + \{V\}\{N_y\}^T)\big]\, dxdy \end{aligned}$$

$$= [K_{zt}]^T \tag{51}$$

$$\begin{aligned} [K_{zz}(\boldsymbol{E})] = \sum_e \iint_e \big[& n^2 k_0^2 (\{N\}\{N\}^T \\ & - \{N_x\}\{N_x\}^T \\ & - \{N_y\}\{N_y\}^T)\big]\, dxdy \end{aligned} \tag{52}$$

$$\begin{aligned} [M_{tt}] = \sum_e \iint_e \big[& (\{U\}\{U\}^T \\ & + \{V\}\{V\}^T)\big]\, dxdy \end{aligned} \tag{53}$$

The integrants in (64) to (67) are given as the functions of the area coordinates, and thus, the numerical integration formulae derived by Hammer

et al. [14], [26], [27] can be directly applied. The integral calculations needed for constructing the matrices $[K_{tt}]$, $[K_{tz}]$, $[K_{zt}]$, $[K_{zz}]$, and $[M_{tt}]$ can be replaced with simple product-sum calculations [14].

From the eigenvector solution, the normalized electric fields vector is obtained. To obtain the intensity-dependent refractive index, it is necessary to compute the actual electric field vector without normalization. The relation between the actual ($\boldsymbol{E}$) and the normalized ($\boldsymbol{e}$) fields can be written as

$$\boldsymbol{E} = \left(\sqrt{P/\widehat{P}}\right)\boldsymbol{e} \tag{54}$$

with

$$\widehat{P} = \mathrm{Re}\left[\frac{j}{2k_0 Z_0}\iint_\Omega \boldsymbol{e}\times(\nabla\times\boldsymbol{e})^*\cdot\boldsymbol{i}_z dxdy\right] \tag{55}$$

$$= \frac{1}{2k_0 Z_0}(\beta\{e_t\}^T[M_{tt}]\{e_t\} + \{e_t\}^T[K_{tz}]\{e_z\}) \tag{56}$$

where Z_0 is the free-space impedance, $\boldsymbol{i}_z$ is the unit vector in the z direction, and the normalized field $\boldsymbol{e}$ is expanded as

$$\boldsymbol{e} = \begin{bmatrix} e_x \\ e_y \\ e_z \end{bmatrix} = \begin{bmatrix} \{U\}^T\{e_t\}_e \\ \{V\}^T\{e_t\}_e \\ j\{N\}^T\{e_z\}_e \end{bmatrix} \tag{57}$$

Equation (49) is a nonlinear generalized eigenvalue problem whose eigenvalue and eigenvector correspond to β^2 and $\boldsymbol{e}$, respectively. Hence, one can solve it self-consistently using the following iterative scheme:

1) Specify the refractive index n, the wavelength $\lambda = 2\pi/k_0$, and optical power P as input data.

2) Assign initial values to β and $\boldsymbol{e}$.

3) To obtain the nonlinear coefficient matrices $[K(\boldsymbol{E})]$ and $[M(\boldsymbol{E})]$, calculate $\boldsymbol{E}$ and n.

4) To obtain a new set of β and $\boldsymbol{e}$, solve the matrix eigenvalue equation (49).

5) Iterate the above procedures 2), 3), and 4) until the solution (eigenvalue) converges within the desired criterion.

Optical power specified in this iterative scheme is increased or decreased between a certain range with appropriate intervals. For the linear case, the solution can be obtained without assigning initial values, and for the nonlinear case, the initial values at each optical power are assigned to the convergent solutions calculated at the previous power. These initial values differ between increasing and decreasing power, and thus, the above iteration scheme can evaluate the hysteresis nature of nonlinear optical waveguides as described later.

4.4 Numerical Results and Discussion

4.4.1 Nonlinear Optical Fiber

We consider a nonlinear optical fiber as shown in Fig. 20. Here, we subdivide a half of the fiber cross section into 180 elements as shown in Fig. 21, and in order to deal with the TE-like (LP^x) modes, the magnetic wall is imposed on the computational window edge AB that is parallel to x-axis.

Figure 22 shows power dispersion curves for the LP^x_{01} mode of a nonlinear optical fiber with saturable nonlinearity in the cladding, where the wavelength $\lambda = 1.3\mu$m, the core diameter is 5 μm, and the following waveguide parameters are used:

$$n = \begin{cases} 1.57 & \text{(core)} \\ n_1 + \Delta n_{sat} \\ \times \left\{ 1 - \exp\left(-\dfrac{n_1 n' |\boldsymbol{E}|^2}{2\Delta n_{sat} Z_0} \right) \right\} \\ & \text{(cladding)} \end{cases}$$

with

$$n_1 = 1.55 \ , \ n' = 10^{-9}\mathrm{m}^2/\mathrm{W} \ , \ \Delta n_{sat} = 0.04.$$

Here, n_1 is the linear part of the nonlinear refractive index, n' is the nonlinear optical coefficient, and Δn_{sat} is the saturation of the nonlinearity.

The change in the effective index with optical power is initially slower, but above a certain threshold the symmetry of the mode is broken and the

field is localized near the core-cladding boundary in nonlinear cladding, causing a jump in the effective index. When decreasing optical power, the dispersion curve exhibits the hysteresis nature and the mode returns abruptly to the linear core. The results using the present VFEM approach agree well with those of approximate scalar finite element method (SFEM) [14].

Figures 23 and 24 show, respectively, the field distributions derived by the SFEM and VFEM, where optical power $P = 0.5\text{mW}$ and 5.5mW. When optical power is below the threshold, most of the power is within the core region, but when optical power increases beyond the threshold, the symmetry-breaking behaviour is observed, suddenly most of the power moves to the cladding, the power inside the core falls drastically, and the field becomes axially asymmetric. The field patterns of SFEM are similar to those of VFEM, and the validity of SFEM is found not only in the low-power region, but in the high-power regime.

4.4.2 Strip-loaded Nonlinear Optical Channel Waveguide

We consider a strip-loaded nonlinear optical channel waveguide as shown in Fig. 25 [16]. Here, we subdivide a half of the waveguide cross section into 252 to 292 elements as shown in Fig. 26, and in order to deal with the fundamental TE-like (E_{11}^{x}) and TM-like (E_{11}^{y}) modes, the electric and magnetic walls are imposed on the computational window edge AD, respectively. The wavelength is $\lambda = 0.515\mu\text{m}$ and the following waveguide parameters are used:

$$n_c = 1.0,\ n_f = 1.57,\ n_s = 1.55$$

$$n = n_1 + \Delta n_{sat}\left\{1 - \exp\left(-\frac{n_1 n' |\boldsymbol{E}|^2}{2\Delta n_{sat} Z_0}\right)\right\}$$

with

$$n_1 = 1.55\ ,\ n' = 10^{-9}\text{m}^2/\text{W}\ ,\ \Delta n_{sat} = 0.2.$$

Figure 27 shows power dispersion curves for the E_{11}^{x} and E_{11}^{y} modes. Hysteresis loops are observed in the dispersion curves for linear-strip thickness $t = 8$ and $10\mu\text{m}$ (see Figs. 27(b) and (c)). The results of the present VFEM approach agree well with those of the conventional penalty VFEM approach [16]. In [19] only the results for the E_{11}^{x} mode are presented.

Quite well agreement between the VFEM and SFEM results is also observed in the low-power regime. However, a great discrepancy is found between the VFEM and SFEM results in the high-power region, and the modal birefringence is enhanced in the SFEM calculation, showing that the scalar field theory cannot predict accurately the modal birefingence of nonlinear optical channel waveguides.

4.4.3 MQW-embedded Nonlinear Optical channel Waveguide

In order to discuss the limitations of the scalar field theory in detail, we consider MQW-embedded nonlinear optical channel waveguides with strong modal birefringences as shown in Fig. 28, where the wavelength $\lambda = 0.820\mu$m and the following waveguide parameters are used:

$$W = 1.0\mu\text{m},\ t = 1.0\mu\text{m}$$
$$n_w = n_1 + \Delta n_{sat}\left\{1 - \exp\left(-\frac{n_1 n'|\boldsymbol{E}|^2}{2\Delta n_{sat} Z_0}\right)\right\}$$
$$n_b = 3.2,\ n_s = 3.3,\ n_c = 3.15$$

with

$$n_1 = 3.5\ ,\ n' = 1.305 \times 10^{-8}\text{m}^2/\text{W}\ ,\ \Delta n_{sat} = 0.2$$

where the numbers of the well and barrier layers are N_w and $N_b = N_w - 1$, respectively. Here, we subdivide a quarter of the waveguide cross section, and the magnetic and electric walls are imposed on the computational window edges, considering the TE-like and/or TM-like polarizations.

We can control the modal birefringence by choosing the number of well layers N_w. Fig. 29 shows power dispersion curves for the E_{11}^x and E_{11}^y modes. For a large number of layers, $N_w = 21$ and 11, the results of SFEM agree well with those of VFEM. For a small number of layer, $N_w = 1$, on the other hand, the modal birefringence of SFEM is larger than that of VFEM, reflecting the previous results shown in Fig. 27. The scalar field theory may be applicable to MQW-embedded nonlinear optical waveguides with a large number of layers.

4.5 Conclusion

A self-consistent full-vectorial finite element approach for the modal analysis of nonlinear optical channel waveguides was newly formulated. To

confirm the validity of the newly formulated full-wave approach, nonlinear dispersion characteristics were calculated for various 3-dimensional optical waveguides. A comparison was made with results of a simple scalar finite element method, and it was found that the scalar field theory is appropriate in the low-power regime which does not stimulate the intensity-dependent refractive-index nonlinearity and that for nonlinear optical waveguides with a small number of layers the modal birefringence is overestimated with the approximate scalar theory.

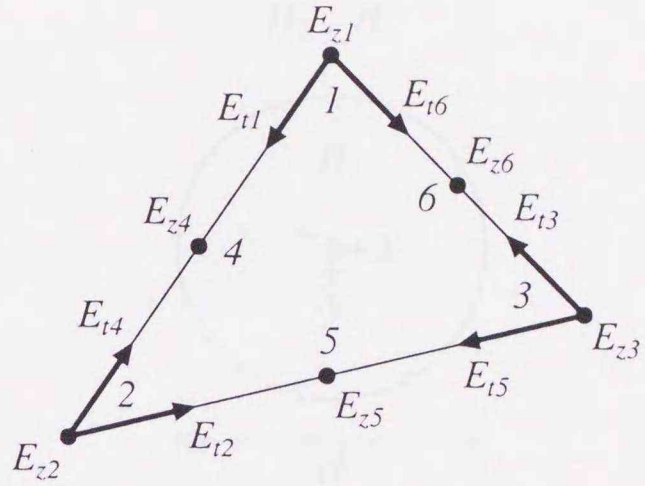

Fig. 19 High-order hybrid edge/nodal triangular element.

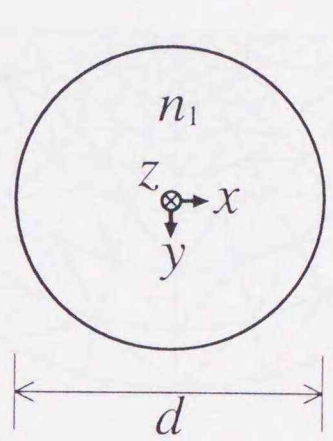

Fig. 20 Nonlinear optical fiber.

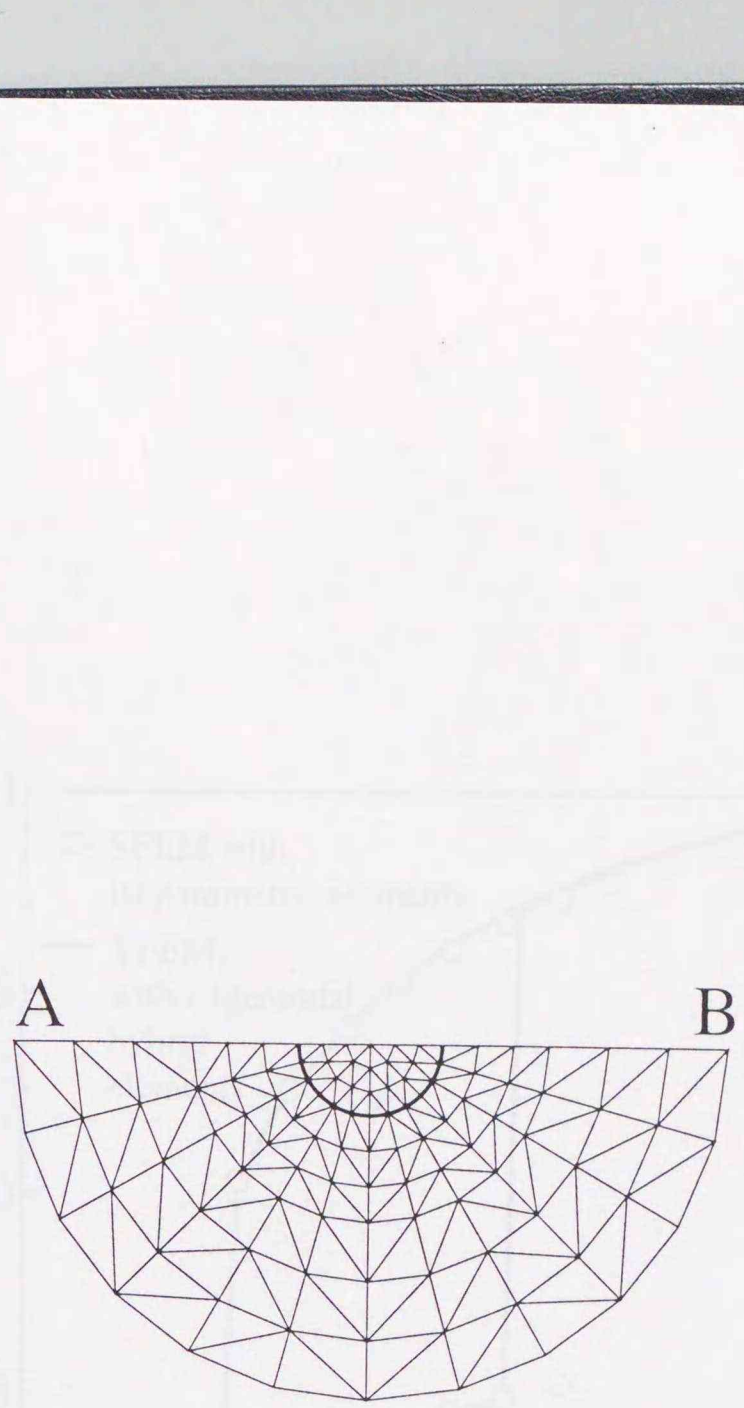

Fig. 21 Element division profile.

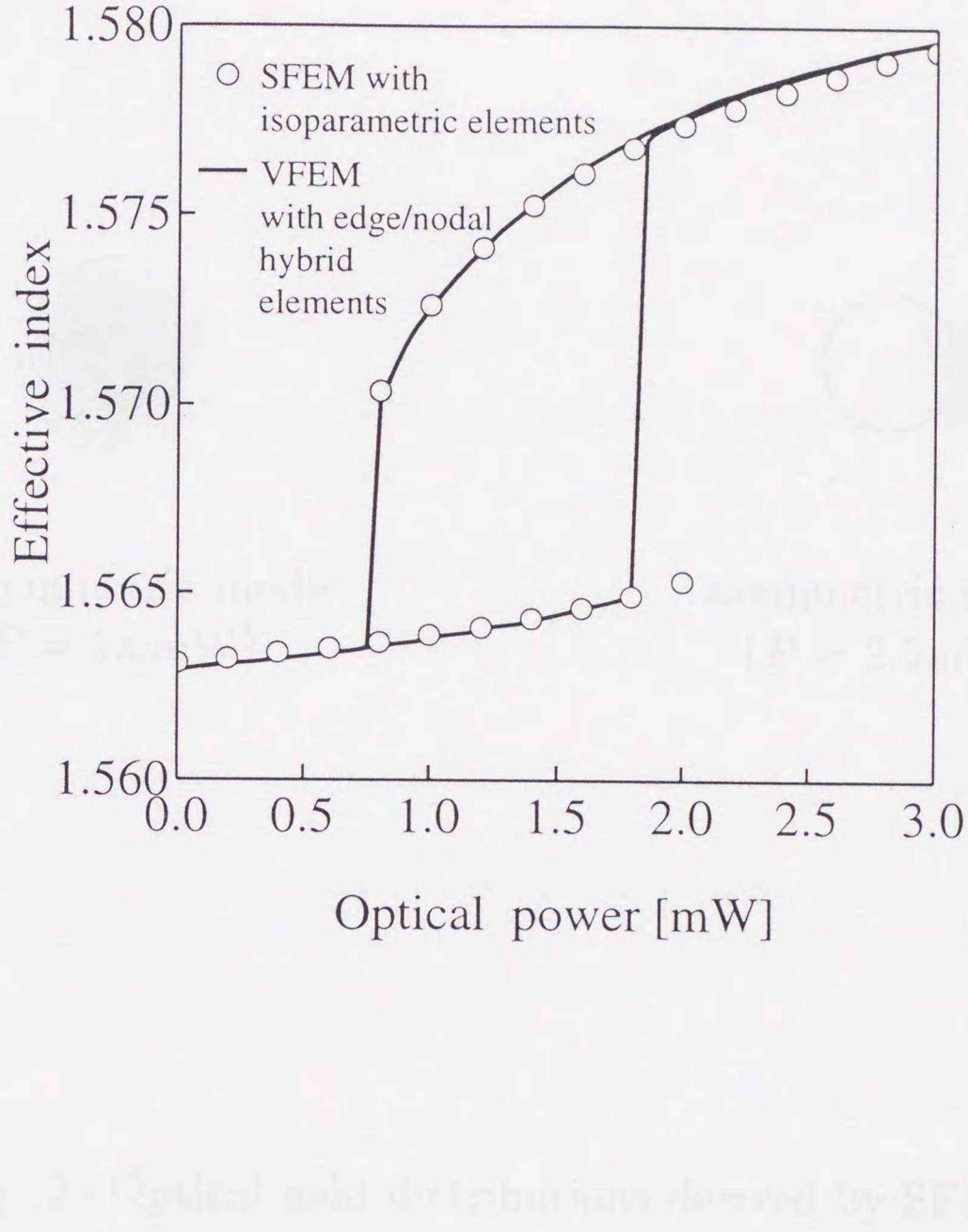

Fig. 22 Power dispersion curves for the LP_{01}^{x} mode of a nonlinear optical fiber with saturable nonlinearity in the cladding.

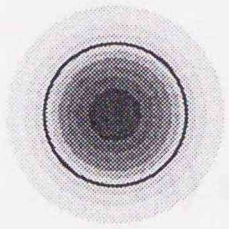

(a) symmetric mode
($P = 1.0\text{mW}$)

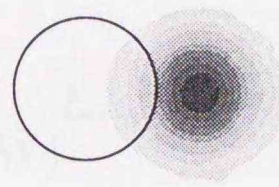

asymmetric mode
($P = 2.5\text{mW}$)

Fig. 23 Optical field distributions derived by SFEM.

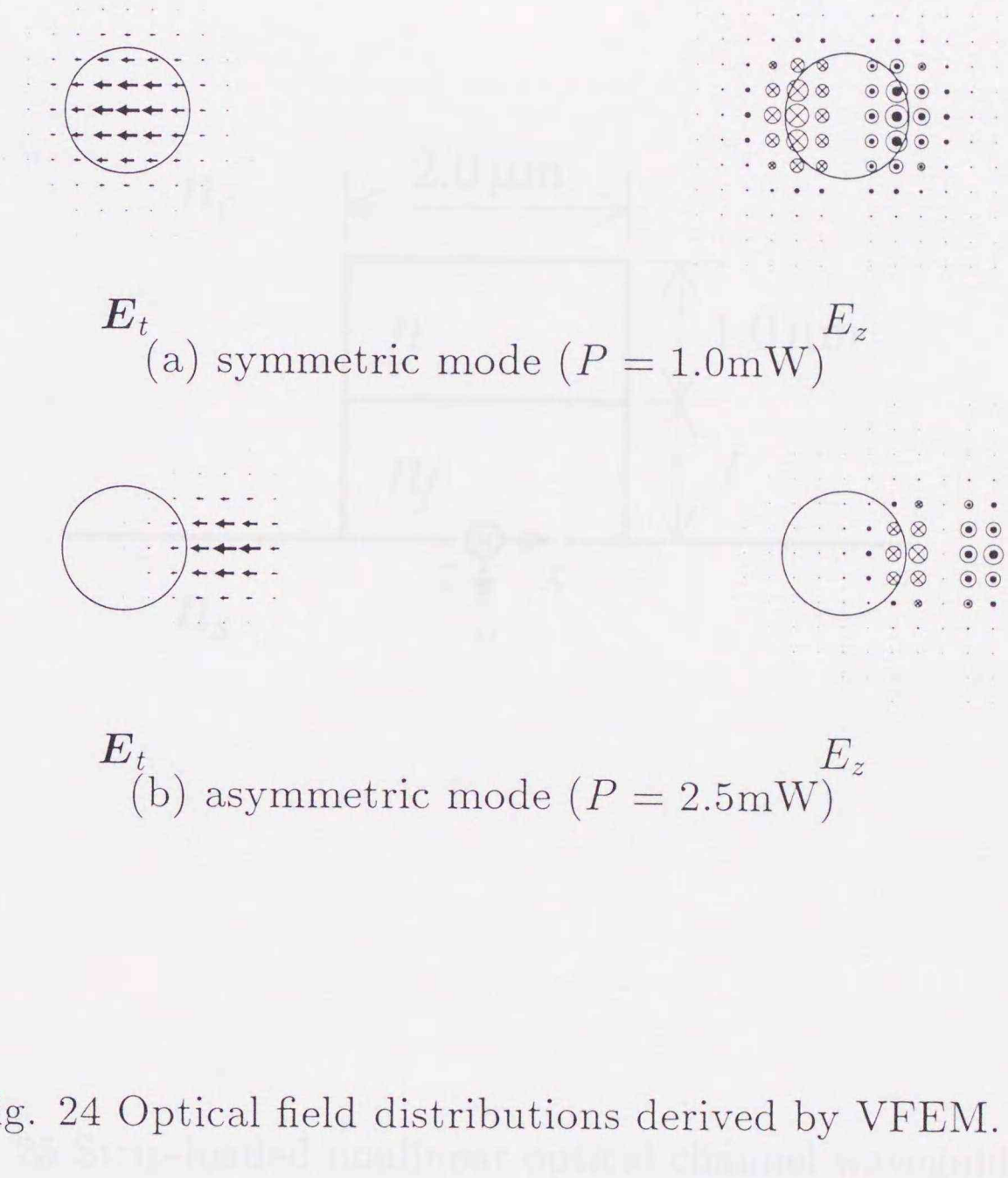

Fig. 24 Optical field distributions derived by VFEM.

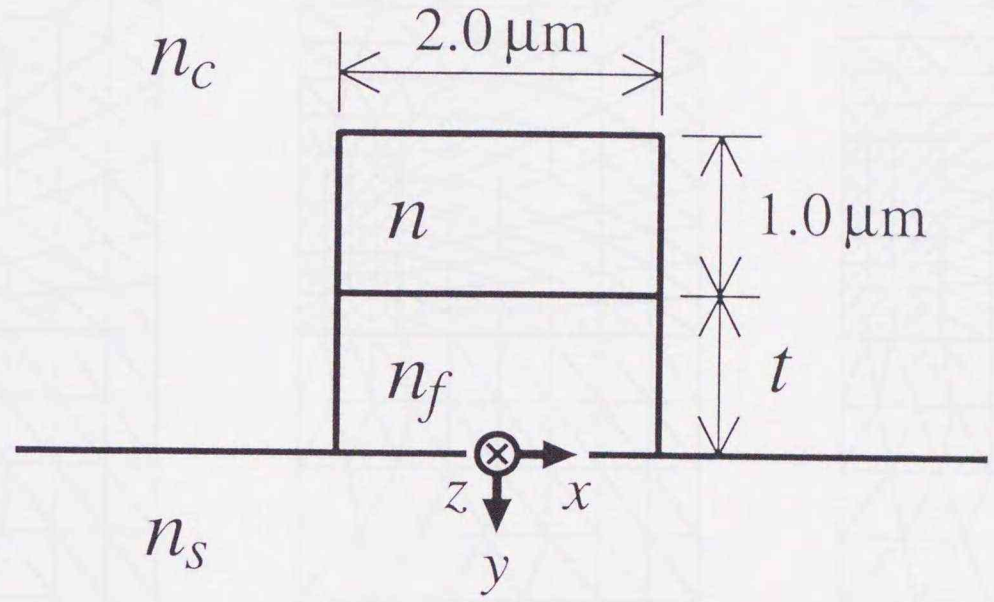

Fig. 25 Strip-loaded nonlinear optical channel waveguide.

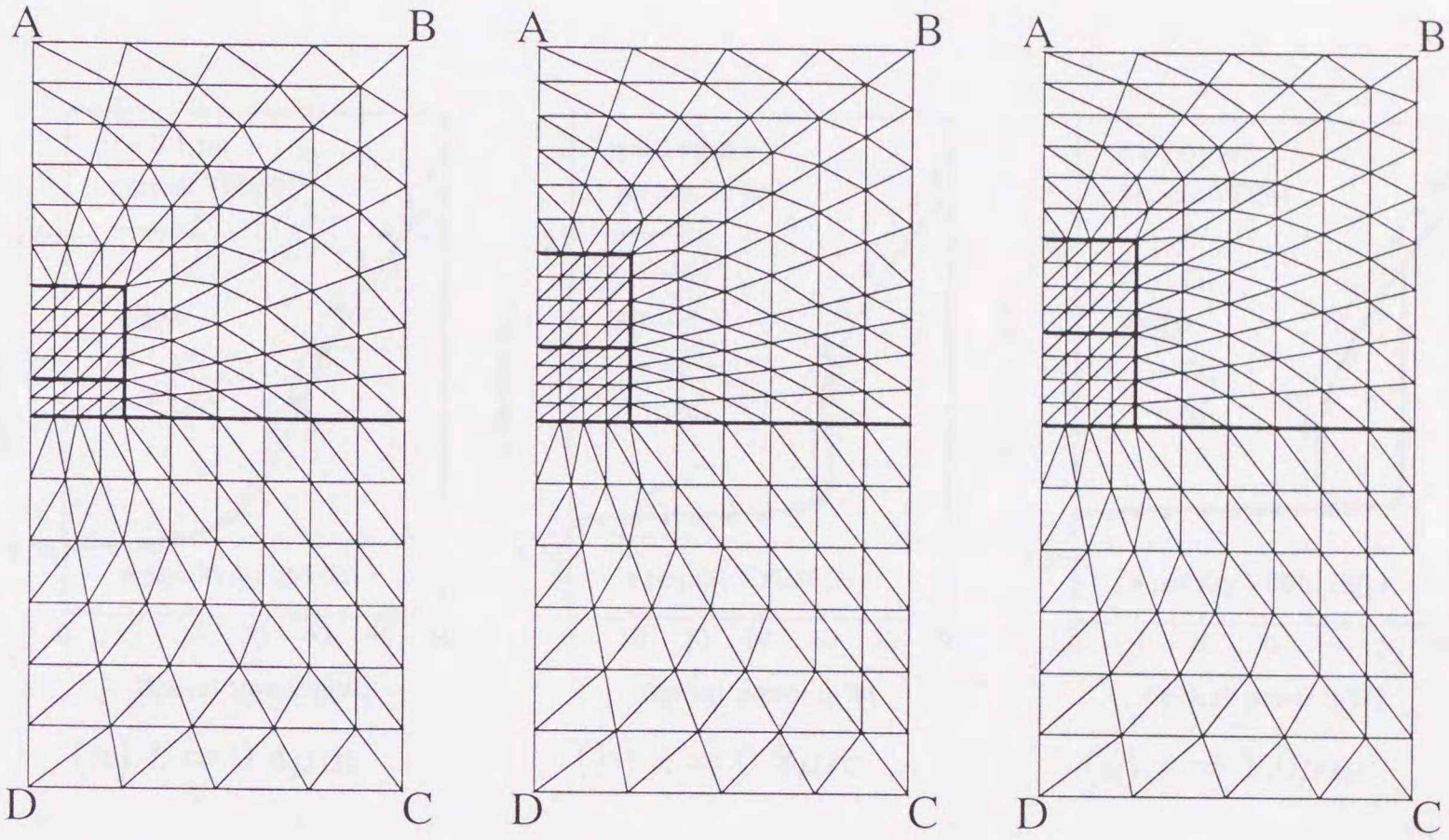

(a) $t = 0.4\mu$m (b) $t = 0.8\mu$m (c) $t = 1.0\mu$m

Fig. 26 Element division profiles for strip-loaded nonlinear optical channel waveguides.

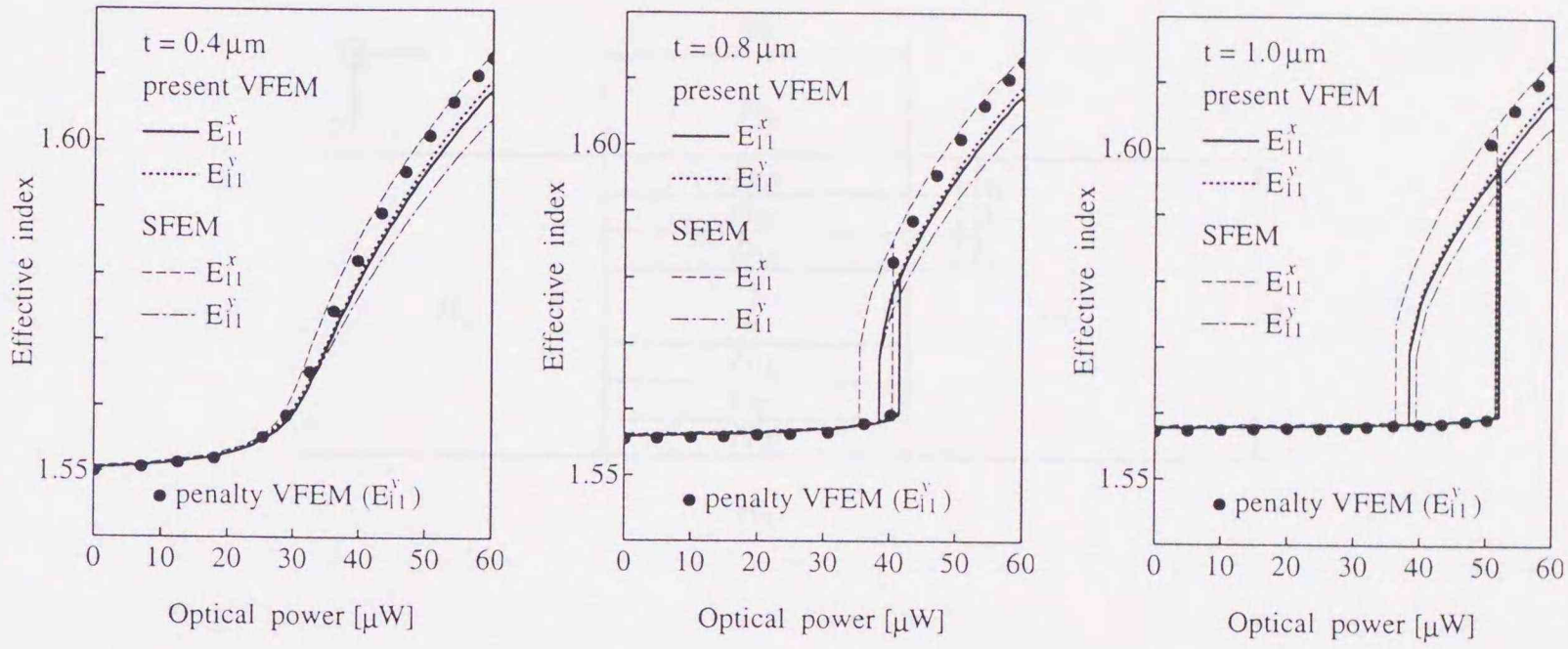

(a) $t = 0.4\mu$m (b) $t = 0.8\mu$m (c) $t = 1.0\mu$m

Fig. 27 Power dispersion curves for the E_{11}^x and E_{11}^y modes of strip-loaded nonlinear optical channel waveguides.

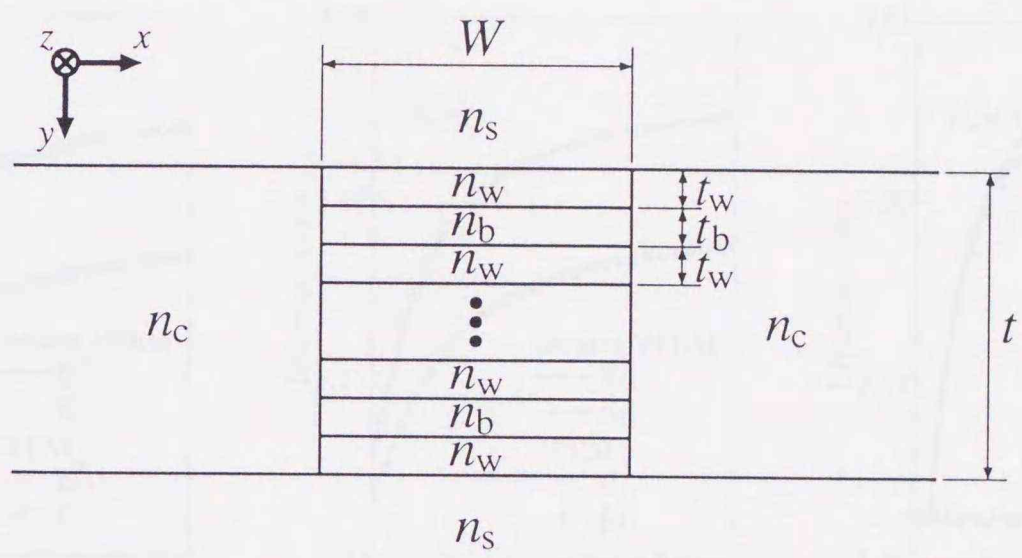

Fig. 28 MQW-embedded nonlinear optical channel waveguide.

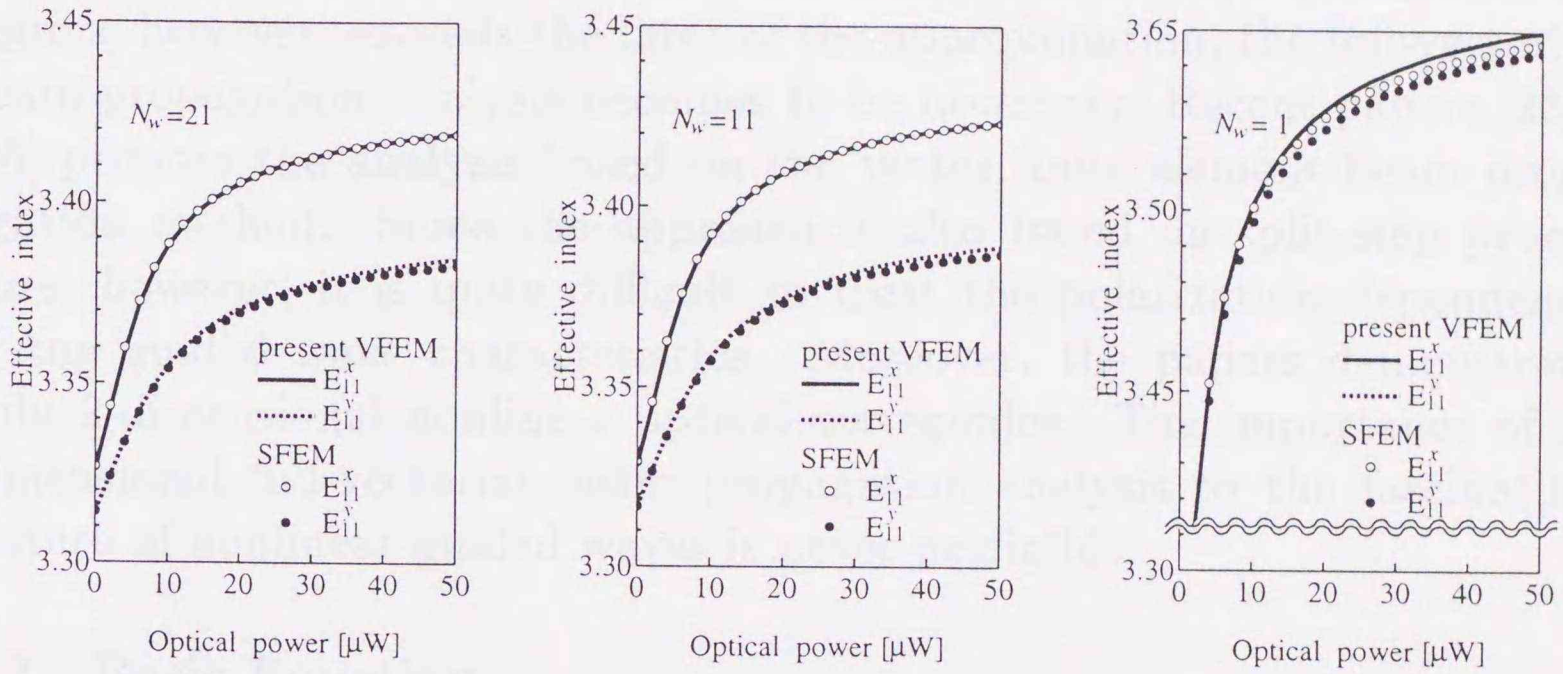

(a) $N_w = 21$ (b) $N_w = 11$ (c) $N_w = 1$

Fig. 29 Power dispersion curves for the E_{11}^x and E_{11}^y modes of MQW-embedded nonlinear optical channel waveguides.

5 Vector Finite Element Beam Propagation Analysis of 3-Dimensional Nonlinear Optical Wavegudes

5.1 Introduction

The 3-dimensional beam propagation analysis with approximated-scalar finite-element and finite-difference methods, described in Chapter 3 of this paper, is available under the assumption of the nonlinear guided wave as a scalar field. When the guided wave in strong-nonlinearity and high-power regims, however, exceeds the limit of the approximation, the full-vectorial beam propagation analysis becomes to be necessary. Recent papers [23]–[25] propose the analysis based on the vector finite element beam propagation method. Since the approach is also based on split-step procedure, however, it is quite difficult to treat the polarization dependence of the guided wave characteristics. Moreover, the papers demonstrate only 2-dimensional nonlinear optical waveguides. The importance of 3-dimensional full-vectorial beam propagation analysis to the fascinating feature of nonlinear guided waves is never negligible.

5.2 Basic Equations

We consider a nonlinear optical waveguide with cross section in the xy plane. From Maxwell's equations, the following vectorial wave equation for the electric field vector $\boldsymbol{E}$ is derived:

$$\nabla \times \nabla \times \boldsymbol{E} - k_0^2 n^2 \boldsymbol{E} = 0 \tag{58}$$

where k_0 is the free space wavenumber and n is the intensity-dependent nonlinear refractive index expressed as

$$n = n(x, y\ ;\ |\boldsymbol{E}|^2). \tag{59}$$

The functional for this wave equation is given by

$$F = \iint_\Omega [(\nabla \times \boldsymbol{E})^* \cdot (\nabla \times \boldsymbol{E}) - k_0^2 n^2 \boldsymbol{E}^* \cdot \boldsymbol{E}] dx dy \tag{60}$$

where $*$ denotes complex conjugate.

5.3 Finite Element Discretization

Dividing the waveguide cross section into a number of high-order hybrid edge/nodal triangular elements [21], [22] as shown in Fig. 30, the electric field vector $\boldsymbol{E}$ in each element is expressed as

$$\boldsymbol{E} = \begin{bmatrix} \{U\} & \{V\} & \{0\} \\ \{0\} & \{0\} & \{N\} \end{bmatrix}^T \begin{bmatrix} \{E_t(z)\}_e \\ j\{E_z(z)\}_e \end{bmatrix} \exp(-jk_0 n_0 z) \tag{61}$$

where $\{U\}$ and $\{V\}$ are the shape function vectors for the linear edge element, $\{N\}$ is the ordinary shape function vector for the quadratic nodal element, T denotes a transpose, $\{E_t\}_e$ is the edge variables in the transverse plane for each element, and $\{E_z\}_e$ is the nodal axial-field vector for each element. More detailed informations about the formulation of the vector finite element method (VFEM) with high-order hybrid edge/nodal triangular elements can be found in [21].

Applying the finite element technique to (60), we obtain the following matrix equation:

$$[K_{tt}]\{E_t\} + \left(\frac{d^2}{dz^2} - 2jk_0 n_0 \frac{d}{dz} - k_0^2 n_0^2\right)[M_{tt}]\{E_t\} - \left(j\frac{d}{dz} + k_0 n_0\right)[K_{tz}]\{E_z\} = \{0\} \tag{62}$$

$$-\left(j\frac{d}{dz} + k_0 n_0\right)[K_{zt}]\{E_t\} + [K_{zz}]\{E_z\} = \{0\} \tag{63}$$

with

$$[K_{tt}(\boldsymbol{E})] = \sum_e \iint_e \left[n^2 k_0^2 (\{U\}\{U\}^T + \{V\}\{V\}^T) + (\{U_y\} - \{V_x\}) \times (\{V_x\}^T - \{U_y\}^T)\right] dxdy \tag{64}$$

$$[K_{tz}] = \sum_e \iint_e \left[(\{U\}\{N_x\}^T + \{V\}\{N_y\}^T)\right] dxdy = [K_{zt}]^T \tag{65}$$

$$[K_{zz}(\boldsymbol{E})] = \sum_e \iint_e \left[n^2 k_0^2 (\{N\}\{N\}^T\right.$$

$$-\{N_x\}\{N_x\}^T$$
$$-\{N_y\}\{N_y\}^T)\big]\,dxdy \tag{66}$$

$$[M_{tt}] = \sum_e \iint_e \big[(\{U\}\{U\}^T$$
$$+\{V\}\{V\}^T)\big]\,dxdy \tag{67}$$

Equation (62) can be rewritten formally as

$$-2jk_0n_0[M_{tt}]\frac{d}{dz}\{E_t\} = \tag{68}$$

$$-\frac{([K_{tt}]-k_0^2n_0^2[M_{tt}])\{E_t\}-k_0n_0[K_{tz}]\{E_z\}-j[K_{tz}]\frac{d}{dz}\{E_z\}}{1-\frac{1}{2jk_0n_0}\frac{d}{dz}} \tag{69}$$

Utilizing Padé approximation [36]–[41] and replacing $(d^2/dz^2)\{E_t\}$ in (62) by

$$[M_{tt}]\frac{d^2}{dz^2}\{E_t\} \simeq -j\frac{1}{2k_0n_0}([K_{tt}]-k_0^2n_0^2[M_{tt}])\frac{d}{dz}\{E_t\}+j\frac{1}{2}[K_{tz}]\frac{d}{dz}\{E_z\} \tag{70}$$

the following Padé equation is obtained from (62) and (63):

$$-j\begin{bmatrix}2k_0n_0[\widetilde{M}_{tt}] & [\widetilde{K}_{tz}]\\ [K_{zt}] & [0]\end{bmatrix}\frac{d}{dz}\begin{bmatrix}\{E_t\}\\ \{E_z\}\end{bmatrix}$$
$$+\begin{bmatrix}[K_{tt}]-k_0^2n_0^2[M_{tt}] & -k_0n_0[K_{tz}]\\ -k_0n_0[K_{zt}] & [K_{zz}]\end{bmatrix}\begin{bmatrix}\{E_t\}\\ \{E_z\}\end{bmatrix}=\begin{bmatrix}\{0\}\\ \{0\}\end{bmatrix} \tag{71}$$

with

$$[\widetilde{M}_{tt}] = [M_{tt}]+\frac{1}{4k_0^2n_0^2}([K_{tt}]-k_0^2n_0^2[M_{tt}]) \tag{72}$$

$$[\widetilde{K}_{tz}] = \frac{1}{2}[K_{tz}] \tag{73}$$

The Fresnel or paraxial equation is easily obtained from (71) by replacing the matrix $[\widetilde{M}_{tt}]$ and $[\widetilde{K}_{tz}]$ by $[M_{tt}]$ and $[K_{tz}]$, respectively.

5.4 Crank-Nicholson Algorithm

Applying the Crank-Nicholson algorithm for the propagation direction, z, to (71) yields

$$[A(\phi)]_i\{\phi\}_{i+1} = [B(\phi)]_i\{\phi\}_i \tag{74}$$

with

$$[A(\phi)]_i = -j\begin{bmatrix} 2k_0 n_0[\widetilde{M}_{tt}]_i & [\widetilde{K}_{tz}]_i \\ [K_{zt}]_i & [0] \end{bmatrix} + 0.5\Delta z \begin{bmatrix} [K_{tt}]_i - k_0^2 n_0^2 [M_{tt}]_i & -k_0 n_0 [K_{tz}]_i \\ -k_0 n_0 [K_{zt}]_i & [K_{zz}]_i \end{bmatrix} \tag{75}$$

$$[B(\phi)]_i = -j\begin{bmatrix} 2k_0 n_0[\widetilde{M}_{tt}]_i & [\widetilde{K}_{tz}]_i \\ [K_{zt}]_i & [0] \end{bmatrix} - 0.5\Delta z \begin{bmatrix} [K_{tt}]_i - k_0^2 n_0^2 [M_{tt}]_i & -k_0 n_0 [K_{tz}]_i \\ -k_0 n_0 [K_{zt}]_i & [K_{zz}]_i \end{bmatrix} \tag{76}$$

$$\{\phi\}_i = \begin{bmatrix} \{E_t\}_i \\ \{E_z\}_i \end{bmatrix} \tag{77}$$

where Δz is the propagation step size, and the subscripts i and $i+1$ denote the quantities related to the ith and $(i+1)$th propagation steps, respectively.

The reference refractive index n_0 is renewed at each propagation step automatically as [39]–[41], [44]

$$n_{0,i} = \mathrm{Re}\left[\frac{-b_i + \sqrt{b_i^2 + 4a_i c_i}}{2a_i}\right] \tag{78}$$

with

$$a_i = \{E_t\}_i^\dagger [M_{tt}]_i \{E_t\}_i \tag{79}$$

$$b_i = \{E_t\}_i^\dagger [K_{tz}]_i \{E_z\}_i + \{E_z\}_i^\dagger [K_{zt}]_i \{E_t\}_i \tag{80}$$

$$c_i = \{E_t\}_i^\dagger [K_{tt}]_i \{E_t\}_i \tag{81}$$

where $\dagger$ denotes complex conjugate and transpose.

Equation (74) can be solved with the following iterative scheme:

1) Specify the refractive index n, the wavelength $\lambda = 2\pi/k_0$, and optical power as input data.

2) Assign initial values of the reference refractive index n_0 and the slowly varying complex amplitude $\{\phi\}$.

3) Calculate coefficient matrices $[A]$ and $[B]$ and solve (74) for a new solution $\{\phi\}_{i+1}$.

4) Update n from (59) and n_0 from (78).

5) Iterate the above procedure 2), 3), and 4) until we reach the desired number of iterations in the z direction.

5.5 Numerical Results and Discussion

5.5.1 Beam Propagation Analysis of Nonlinear Optical Fiber

The modal analysis [14] can be easily performed by setting $d/dz = 0$ in (62), and then n_0 becomes the modal effective index, n_{eff}, and $\{\phi\}$ is the corresponding modal (stationary) field. An iterative scheme for solving this nonlinear generalized eigenvalue problem has already been reported in [14]. We consider a nonlinear optical fiber as shown in Fig. 31. Here, we subdivide all the fiber cross section into 360 hybrid elements (Fig. 32), and in order to deal with the TE-like (LP^x) modes, the magnetic wall is imposed on the computational window edge AB that is parallel to x-axis.

Figure 33 shows the contour plots of field amplitudes for an optical fiber with Kerr nonlinearity in the core, where the input LP_{01}-beam power $P = 0.5\text{mW}$, the wavelength $\lambda = 0.5145\mu\text{m}$, the core diameter $a = 2\mu\text{m}$, the refractive index of the cladding $n_2 = 1.55$, and the refractive index of the core is given by

$$n_1 = 1.57[1 + n'|\boldsymbol{E}|^2/(2Z_0)] \ , \ n' = 10^{-9}\ \text{m}^2/\text{W}.$$

In this input power, the excited beam is propagating stably up to the distance $l = 200\mu\text{m}$, and the beam profile is quite similar to that of the nonlinear LP_{01} field at this input power $P = 0.5\text{mW}$, and these results show the validity of this beam propagation approach.

5.6 Conclusion

We have newly formulated an efficient 3-dimensional beam-propagation approach based on the Crank-Nicholson finite element method for the analysis of nonlinear optical fibers. Using the numerical approach developed here, propagation characteristics of optical fibers with nonlinear core and linear cladding have been analyzed by launching the linear LP_{01} beam. We have confirmed the validity of this beam propagation approach, in comparison with the field profile of propagating beams and nonliear LP_{01} modes

in the nonlinear fiber. By the use of this numerical techinique, unique features of nonlinear optical waveguides and devices are now investigated and the results will be reported in near future.

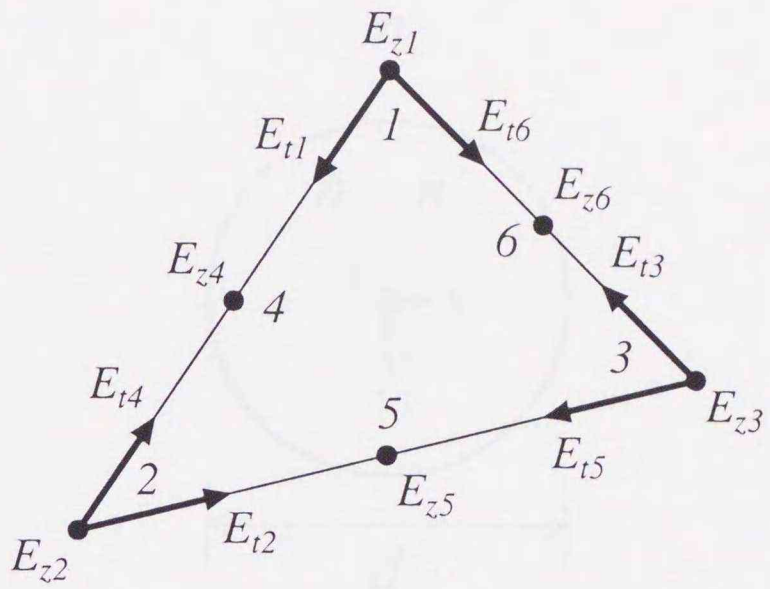

Fig. 30 Edge and nodal hybrid elements.

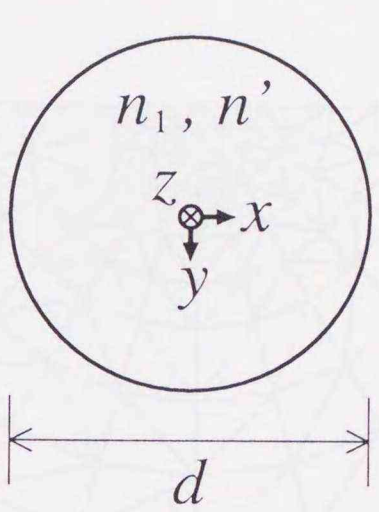

Fig. 31 Nonlinear optical fiber with nonlinear core and linear cladding.

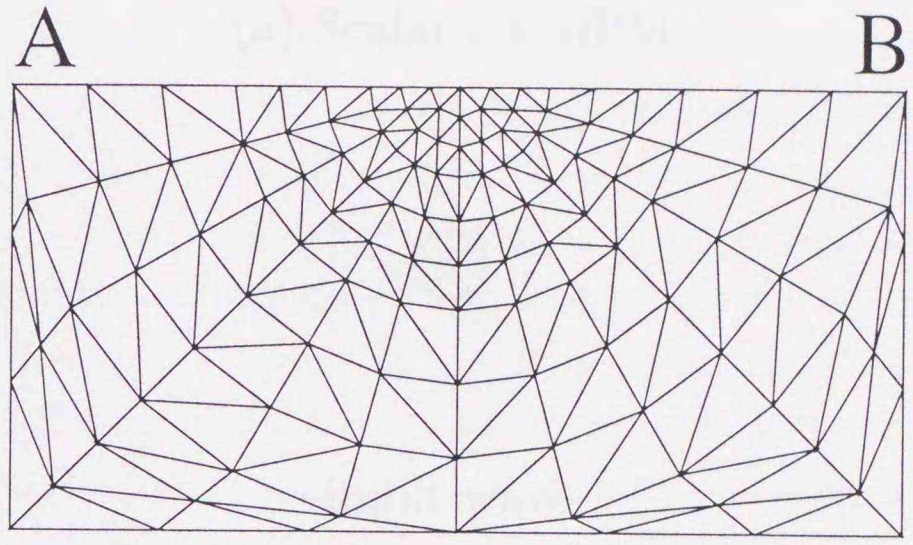

Fig. 32 Element division profile.
(216 elements)

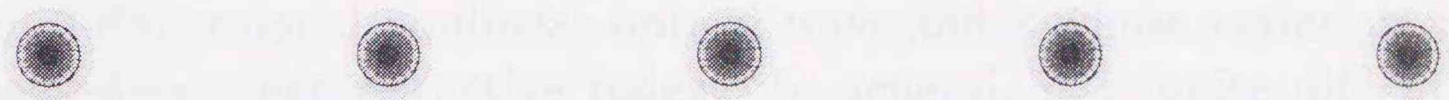

input wave l =50μm l =100μm l =150μm l =200μm

(a) Scalar FE-BPM

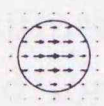

input wave

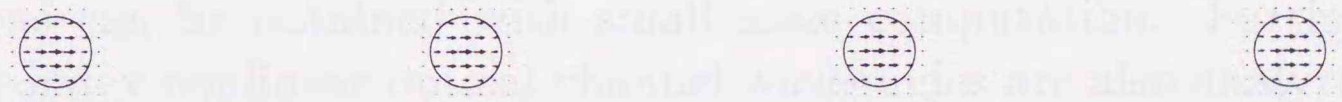

l =25μm l =50μm l =75μm l =100μm

l =125μm l =150μm l =175μm l =200μm

(b) Vector FE-BPM ($\boldsymbol{E}_t$)

Fig. 33 Electric Field Distribution
(P = 0.5 mW)

6 Summary

This research has proposed and has formulated the numerical approaches based on the finite element method for modal and beam-propagation analysis of 3-dimensional nonlinear optical waveguides whose materials have intensity-dependent refractive index. In general, it is quite difficult or sometimes impossible without applying the numerical approach to assess the unique phenomena of nonlinear guided waves such as optical bistability, axially asymmetric modes in cylindrical optical waveguides, spatial soliton emission, and so on. Hence these proposed numerical approaches reveal the interesting feature of nonlinear optical waveguides and integrated nonlinear optics.

In chapter 2, a self-consistent numerical approach based on the scalar finite element method is described for the analysis of both TE-like and TM-like nonlinear guided waves in optical channel waveguides. In order to improve the convergence and accuracy of solutions, isoparametric elements and numerical integration formulae derived by Hammer *et al.* are introduced. Numerical results are presented for nonlinear elliptical core optical fibers, and it is confirmed that in this approach, highly accurate solutions can be obtained with small scale computation. Furthermore, graded-index nonlinear optical channel waveguides are also analyzed, and the influence of refractive-index profiles on propagation characteristics of the nonlinear guided waves is investigated.

In chapter 3, a 3-dimensional beam propagation method is described for the analysis of nonlinear optical fibers, where the finite element and finite difference methods are, respectively, utilized for discretizing the fiber cross section and the propagation direction. For efficient evaluation of wide-angle beam propagation, Padé approximation is applied to the differential operator along the propagation direction. In order to improve the efficiency and accuracy of solutions, isoparametric elements and numerical integration formulae derived by Hammer *et al.* are introduced. The propagation characteristics of nonlinear optical fibers with linear core and nonlinear cladding are analyzed, and unique features of nonlinear guided-wave propagation are investigated. Furthermore, all-optical logic gates with practical, 3-dimensional geometry consisting of optical fibers and a nonlinear film are proposed, and their operations of Boolean arithmetric

are demonstrated.

In chapter 4, a self-consistent full-vectorial approach based on the finite element method is described for the modal analysis of nonlinear optical channel waveguides, and an application of conventional scalar field theory to the prediction of modal properties of both TE-like and TM-like nonlinear guided modes is examined. Numerical results are presented for nonlinear optical fibers, strip-loaded nonlinear optical channel waveguides, and multiple-quantum-well-embedded nonlinear optical channel waveguides. Serious limitations on the validity of the scalar field approximation are found in the high power regime, where nonlinearities are expected to play an essential role in forming the stationary mode.

In chapter 5, a 3-dimensional full-vectorial beam propagation method is described for the analysis of nonlinear optical waveguides, where the finite element and finite difference methods are, respectively, utilized for discretizing the waveguide cross section and the propagation direction. In order to improve the efficiency and accuracy of solutions, isoparametric elements and numerical integration formulae derived by Hammer *et al.* are introduced.

These numerical techniques based on the finite element method developed in this research will be applied successfully to the computer-aided design for nonlinear optical waveguides and integrated nonlinear optical devices.

Acknowledgements

I would like to express my sincere appreciation to Professor Masanori Koshiba and Associate Professor Yasuhide Tsuji, Division of Electronics and Information Engineering, Graduate School of Engineerning, Hokkaido University, for the continuing guidance and encouragement during my whole research.

I am also grateful to Professor Kiyohiko Itoh, Professor Yasutaka Ogawa, and Professor Yoshikazu Miyanaga, Division of Electronics and Information Engineering, Graduate School of Engineerning, Hokkaido University, for helpful suggestions and observations.

I also wish to acknowledge numerious illuminating discussions of members in our laboratory.

References

[1] J. Chrostowski and S. Chelkowski, "Analysis of an optical rib waveguides with a nonlinear substrate," *Opt. Lett.*, vol. 12, pp. 528–530, July 1987.

[2] G. J. M. Krijnen, H. J. W. M. Hoekstra, and P. V. Lambeck, "A new method for the calculation of propagation constants and field profiles of guided modes of nonlinear channel waveguides based on the effective index method," *J. Lightwave Technol.*, vol. 12, pp. 1550–1559, Sept. 1994.

[3] K. Hayata and M. Koshiba, "Full vectorial analysis of nonlinear-optical waveguides," *J. Opt. Soc. Am. B*, vol. 5, pp. 2494–2501, Dec. 1988.

[4] R. D. Ettinger, F. A. Fernandez, B. M. A. Rahman, and J. B. Davies, "Vector finite element solution of saturable nonlinear strip-loaded optical waveguides," *IEEE Photon. Technol. Lett.*, vol. 3, pp. 147–149, Feb. 1991.

[5] K. Hayata and M. Koshiba, "Self-localization and spontaneous symmetry breaking of optical fields propagating in strongly nonlinear channel waveguides: limitations of the scalar field approximation," *J. Opt. Soc. Am. B*, vol. 9, pp. 1362–1368, Aug. 1992.

[6] X. H. Wang and G. K. Campbrell, "Full vectorial simulation of bistability phenomena in nonlinear-optical channel waveguides," *J. Opt. Soc. Am. B*, vol. 10, pp. 1090–1095, June 1993.

[7] X. H. Wang and G. K. Campbrell, "Simulation of strong nonlinear effects in optical waveguides," *J. Opt. Soc. Am. B*, vol. 10, pp. 2048–2055, Nov. 1993.

[8] Q. Y. Li, R. A. Sammut, and C. Pask, "Variational and finite element analyses of nonlinear strip optical waveguides," *Opt. Commun.*, vol. 94, pp. 37–43, Apr. 1992.

[9] C.T. Seaton, J.D. Valera, R.L. Shoemaker, G.I. Stegeman, J.T. Chilwell, and S.D. Smith, "Calculations of nonlinear TE waves guided

by thin dielectric films bounded by nonlinear media," *IEEE J. Quantum Electron.*, vol. QE–21, pp. 774–783, July 1985.

[10] M.A. Gubbels, E.M. Wright, G.I. Stegeman, C.T. Seaton, and J.V. Moloney, "Numerical study of soliton emission from a nonlinear waveguide," *J. Opt. Soc. Amer. B*, vol. 4, pp. 1837–1842, Nov. 1987.

[11] A.D. Boardman, G.S. Cooper, and D.J. Robbins, "Novel nonlinear waves in optical fibers," *Opt. Lett.*, vol. 11, pp. 112–114, Feb. 1986.

[12] N.N. Akhmediev, R.F. Nabiev, and Yu.M. Popov, "Angle-dependent nonlinear modes of a cylindrical waveguides," *J. Opt. Soc. Amer. B*, vol. 7, pp. 975–980, June 1990.

[13] K. Hayata and M. Koshiba, "Self-localization and spontaneous symmetry breaking of optical fields propagating in strongly nonlinear channel waveguides: limitations of the scalar field approximation," *J. Opt. Soc. Am. B*, vol. 9, pp. 1362–1368, Aug. 1992.

[14] A. Niiyama, M. Koshiba, and Y. Tsuji, "An efficient scalar finite element formulation for nonlinear optical channel waveguides," *J. Lightwave Technol.*, vol. 13, pp. 1919–1925, Sept. 1995.

[15] K. Hayata and M. Koshiba, "Full vectorial analysis of nonlinear-optical waveguides," *J. Opt. Soc. Am. B*, vol. 5, pp. 2494–2501, Dec. 1988.

[16] R. D. Ettinger, F. A. Fernandez, B. M. A. Rahman, and J. B. Davies, "Vector finite element solution of saturable nonlinear strip-loaded optical waveguides," *IEEE Photon. Technol. Lett.*, vol. 3, pp. 147–149, Feb. 1991.

[17] M. Zoboli, F.D. Pasquale, and S. Selleri "Full-vectorial and scalar solutions of nonlinear optical fibers," *Opt. Commun.*, vol. 97, pp. 11–15, Apr. 1993.

[18] X.H. Wang and G.K. Campbrell, "Full vectorial simulation of bistability phenomena in nonlinear-optical channel waveguides," *J. Opt. Soc. Am. B*, vol. 10, pp. 1090–1095, June 1993.

[19] X.H. Wang and G.K. Campbrell, "Simulation of strong nonlinear effects in optical waveguides," *J. Opt. Soc. Am. B*, vol. 10, pp. 2048–2055, Nov. 1993.

[20] S. Selleri and M .Zoboli, "An improved finite element method formulation for the analysis of nonlinear anisotropic dielectric waveguides," *IEEE Trans. Microwave Theory Tech.*, vol. 43, Apr. 1995

[21] M. Koshiba, S. Maruyama, and K. Hirayama, "A vector finite element method with the higher-order mixed-interpolation-type triangular elements for optical waveguiding problems," *J. Lightwave Technol.*, vol. 12, pp. 495–502, Mar. 1994.

[22] M.S. Alam, M. Koshiba, K. Hirayama, and Y. Hayashi, "Hybrid-mode analysis of multilayered and multiconductor transmission lines," *IEEE Trans. MTT*, vol. 45, Feb. 1997.

[23] S.V. Polstyanko, R. Dyczij-Edlinger and J.-F. Lee, "Full wave vector maxwell equation simulation of nonlinear self-forcusing effects in three spatial dimensions," *IEEE. Trans. Magnetics*, vol. 33, no.2, pp. 1780–1783, Mar. 1997.

[24] S.V. Polstyanko, R. Dyczij-Edlinger and J.-F. Lee, "Full vectorial analysis of a nonlinear slab waveguide based on the nonlinear hybrid vector finite element method," *Opt. Lett.*, vol. 21, no. 2, pp. 98–100, Jan. 1996.

[25] S.V. Polstyanko and J.-F. Lee, "Nonlinear hybrid vector finite element method for modeling wave propagation in nonlinear media," *Radio Science*, vol. 31, no. 4, pp.913–922, July–Aug. 1996.

[26] O. C. Zienkiewitz, *The Finite Element Method (3rd Edition)*, London: McGraw-Hill, 1977.

[27] M. Koshiba, *Optical Waveguide Theory by the Finite Element Method*, Tokyo/Dordrecht: KTK Scientific Publishers/Kluwer Academic Publishers, 1992.

[28] K. Hayata, M. Koshiba, and M. Suzuki, "Finite-element solution of arbitrarily nonlinear, graded-index slab waveguides," *Electron. Lett.*, vol. 23, pp. 429–431, Apr. 1987.

[29] K. Hayata, M. Nagai, and M. Koshiba, "Finite-element formalism for nonlinear slab-guided waves," *IEEE Trans. Microwave Theory Tech.*, vol. 36, pp. 1207–1214, Apr. 1987.

[30] K. Ogusu, "Nonlinear TE waves guided by graded-index planar waveguides," *Opt. Commun.*, vol. 63, pp. 380–384, Sept. 1987.

[31] M. R. Ramadas, R. K. Varshney, K. Thyagarajan, and A. K. Ghatak, "A matrix approach to study the propagation characteristics of a general nonlinear planar waveguide," *J. Lightwave Technol.*, vol. 7, pp. 1901–1905, Dec. 1989.

[32] N. Saiga, "Calculation of TE modes in graded-index nonlinear optical waveguides with arbitrary profile of refractive index," *J. Opt. Soc. Am. B*, vol. 8, pp. 88–94, Jan. 1991.

[33] M. De Sario, A. D'Orazio, V. Petruzzelli, and F. Prudenzano, "Propagation characteristics of nonlinear graded-index optical waveguides," *J. Opt. Soc. Am. B*, vol. 10, pp. 1565–1571, Sept. 1993.

[34] M. Koshiba, H. Saitoh, M. Eguchi, and K. Hirayama, "A simple scalar finite element approach to optical rib waveguides," *IEE Proc., pt. J*, vol. 139, pp. 166–171, Apr. 1992.

[35] R. A. Sammut and C. Pask, "Gaussian and equivalent-step-index approximations for nonlinear waveguides," *J. Opt. Soc. Am. B*, vol. 8, pp. 395–402, Feb. 1991.

[36] G.R. Hadley, "Wide-angle beam propagation using Padé approximant operator," *Electron. Lett.*, vol. 25, pp. 1426–1428, Oct. 1992.

[37] W.P. Huang and C.L. Xu, "A wide-angle vector beam propagation method," *IEEE Photon. Technol. Lett.*, vol. 4, pp. 1118–1120, Oct. 1992.

[38] G.R. Hadley, "Multistep method for wide-angle beam propagation," *Opt. Lett.*, vol. 17, pp. 1743–1745, Dec. 1992.

[39] Y. Tsuji, M. Koshiba, and T. Tanabe, "A wide-angle beam propagation method using a finite element scheme," *Trans. IEICE*, vol. J79–C–I, pp. 381–388, Oct. 1996 (in Japanese).

[40] M. Koshiba and Y. Tsuji, "A wide-angle finite-element beam propagation method," *IEEE. Photon. Technol. Lett.*, vol. 8, pp. 1208–1210, Sept. 1996.

[41] Y. Tsuji, M. Koshiba, and T. Shiraishi, "Finite element beam propagation method for three-dimensional optical waveguide structures," *J. Lightwave Technol.*, accepted for publication.

[42] G. Cancellieri, F. Chiaraluse, E. Gambi, and P. Pierleoni, "Coupled-soliton photonic logic gates: practical design procedures," *J. Opt. Soc. Amer. B*, vol. 12, pp. 1300–1306, July 1995.

[43] Y. Arai, A. Maruta, and M. Matsuhara, "Transparent boundary for the finite-element beam-propagation method," *Opt. Lett.*, vol. 18, pp. 765–766, May 1993.

[44] F. Schmidt: "An adaptive approach to the numerical solution of Frensnel's wave equation", *J. Lightwave Technol.*, vol. 11, pp. 1425–1434, Sept. 1993.

[45] D.R. Heatley, E.M. Wright, and G.I. Stegeman, "Soliton coupler," *Appl. Phys. Lett.*, vol. 53, pp. 172-174, July 1988.

List of Author's Publications and Presentations

1) Papers

(1) A. Niiyama, M. Koshiba, and Y. Tsuji, "A scalar finite element analysis of nonlinear optical channel waveguides using isoparametric elements", Trans. IEICE, vol. J78–C–I, pp. 88–95, Feb. 1995 (in Japanese).

(2) A. Niiyama, M. Koshiba, and Y. Tsuji, "An efficient scalar finite element formulation for nonlinear optical waveguides", Journal of Lightwave Technology, vol. 13, pp. 1919–1925, Sept. 1995.

(3) A. Niiyama and M. Koshiba, "3-Dimensional beam propagation analysis of nonlinear optical fibers", IEICE Transactions on Communications, vol. E80–B, pp. 522–527, Apr. 1997.

(4) A. Niiyama and M. Koshiba, "Three-Dimensional beam propagation analysis of nonlinear optical fibers and optical logic gates", Journal of Lightwave Technology, vol. 16, pp. 162–168, Jan. 1998.

(5) T. Yasui, M. Koshiba, A. Niiyama, and Y. Tsuji, "Finite element beam propagation method for nonlinear optical waveguides", Trans. IEICE, vol. J81–C–I, accepted for publication (in Japanese).

2) International Conferences

(1) A. Niiyama and M. Koshiba, "A simple and efficient scalar finite element approach to nonlinear optical channel waveguides", Technical Digest of the Pacific Rim Conference on Lasers and Electro-Optics (CLEO/Pacific Rim '95), pp. 288–289, July 1995.

(2) M. Koshiba and A. Niiyama, "3-Dimensional beam propagation analysis of nonlinear optical fibers", (invited paper) Proceedings of 1997 International Symposium on Nonlinear Theory and Applications (NOLTA '97), pp. 933–936, Nov./Dec. 1997.

3) Techinical Reports

(1) A. Niiyama, M. Koshiba, and Y. Tsuji, "A scalar finite element analysis of nonlinear optical channel waveguides using isoparametric elements", Technical Report of IEICE, OPE94–53, Sept. 1994.

(2) A. Niiyama and M. Koshiba, "3-Dimensional beam propagation analysis of Nonlinear optical fibers", Technical Report of IEEJ/IEICE, EMT–96–73, Oct. 1996.

(3) A. Niiyama and M. Koshiba, "Limitations of approximate scalar theory for 3-D nonlinear optical Waveguides", Technical Report of IEEJ/IEICE, EMT–97–110, Nov. 1997.

4) Domestic Conferences

(1) A. Niiyama, M. Koshiba and Y. Tsuji, "Applicability of isoparametric elements in the finite-element analysis of nonlinear optical channel waveguides", 1994 Joint Convention Record, the Hokkaido Chapters of the Institutes of Electrical and Information Engineers, Japan, 194, Oct. 1994.

(2) A. Niiyama, M. Koshiba, "Finite element analysis of nonlinear optical waveguides using isoparametric elements", Proceedings of the 1995 IEICE General Conference, C-209, Mar. 1995.

(3) A. Niiyama and M. Koshiba, "Gaussian-beam excitation and stability of nonlinear guided waves in elliptical-core optical fibers", 1995 Joint Convention Record, the Hokkaido Chapters of the Institutes of Electrical and Information Engineers, Japan, 190, Oct. 1995.

(4) T. Tsuchiya, A. Niiyama and M. Koshiba, "Birefringence of nonlinear optical channel waveguides with multiple quantum wells", 1995 Joint Convention Record, the Hokkaido Chapters of the Institutes of Electrical and Information Engineers, Japan, 204, Oct. 1995.

(5) T. Tsuchiya, A. Niiyama and M. Koshiba, "Guided modes in nonlinear optical channel waveguides with multiple quantum wells", Proceedings of the 1995 Electronics Society Conference of IEICE, C-202, Sept. 1995.

(6) T. Tsuchiya, A. Niiyama, M. Koshiba, and Y. Tsuji, "Polarization dependence of spatial soliton emission in optical waveguides with a linear core and nonlinear claddings", 1996 Joint Convention Record, the Hokkaido Chapters of the Institutes of Electrical and Information Engineers, Japan, 220, Oct. 1996.

(7) A. Niiyama and M. Koshiba, "3-Dimensional beam propagation analysis of Nonlinear optical fibers", Proceedings of the 1997 IEICE General Conference, SC–13–1, Mar. 1997.

(8) T. Yasui, M. Koshiba, A. Niiyama and Y. Tsuji, "Beam propagation analysis of optical waveguides with linear cores and nonlinear claddings", 1997 Joint Convention Record, the Hokkaido Chapters of the Institutes of Electrical and Information Engineers, Japan, 256, Oct. 1997.

(9) A. Niiyama and M. Koshiba, "Limitations of approximate scalar theory for 3-D nonlinear optical Waveguides", 1997 Joint Convention Record, the Hokkaido Chapters of the Institutes of Electrical and Information Engineers, Japan, 257, Oct. 1997.

(10) A. Niiyama and M. Koshiba, "Limitations of approximate scalar theory for 3-D nonlinear optical Waveguides", Proceedings of the 1998 IEICE General Conference, C–3–82, Mar. 1998.

(11) T. Yasui, M. Koshiba, A. Niiyama and Y. Tsuji, "Finite element beam propagation method for nonlinear optical waveguides", Proceedings of the 1998 IEICE General Conference, C–3–105, Mar. 1998.

inches 1 2 3 4 5 6 7 8

cm 1 2 3 4 5 6 7 8 9 10 11 12 13 14 15 16 17 18 19

Kodak Color Control Patches

Blue Cyan Green Yellow Red Magenta White 3/Color Black

Kodak Gray Scale

C Y M

A 1 2 3 4 5 6 **M** 8 9 10 11 12 13 14 15 **B** 17 18 19